Front. Earth Sci.
https://doi.org/10.1007/s11707-024-1118-x

RESEARCH ARTICLE

Understanding and improving Yangtze River Basin summer precipitation prediction using an optimal multi-Physics ensemble

Yang ZHAO[1], Fengxue QIAO[2,3], Xin-Zhong LIANG (✉)[4,5], Jinhua YU (✉)[6]

1 Climate, Environment and Sustainability Center, Nanjing University of Information Science and Technology, Nanjing 210044, China
2 Key Laboratory of Geographic Information Science (Ministry of Education), East China Normal University, Shanghai 200241, China
3 School of Geographic Sciences, East China Normal University, Shanghai 200241, China
4 Department of Atmospheric and Oceanic Science, University of Maryland, College Park MD 20740, USA
5 Earth System Science Interdisciplinary Center, University of Maryland, College Park MD 20740, USA
6 Key Laboratory of Meteorological Disaster (KLME) (Ministry of Education) / Collaborative Innovation Center on Forecast and Evaluation of Meteorological Disasters (CIC-FEMD), Nanjing University of Information Science and Technology, Nanjing 210044, China

Abstract This study employs the regional Climate-Weather Research and Forecasting model (CWRF) to first investigate the primary physical mechanisms causing biases in simulating summer precipitation over the Yangtze River Basin (YRB), and then enhance its predictive ability through an optimal multi-physics ensemble approach. The CWRF 30-km simulations in China are compared among 28 combinations of varying physics parameterizations during 1980−2015. Long-term average summer biases in YRB precipitation are remotely correlated with those of large-scale circulations. These teleconnections of biases are highly consistent with the observed correlation patterns between interannual variations of precipitation and circulations, despite minor shifts in their primary action centers. Increased YRB precipitation aligns with a southward shifted East Asian westerly jet, an intensified low-level southerly flow south of YRB, and a south-eastward shifted South Asian high, alongside higher moisture availability over YRB. Conversely, decreased YRB precipitation corresponds to an opposite circulation pattern. The CWRF control configuration using the ensemble cumulus parameterization (ECP), compared to other cumulus schemes, best captures the observed YRB precipitation characteristics and associated circulation patterns. Coupling ECP with the Morrison or Morrison-aerosol microphysics and the CCCMA or CAML radiation schemes enhances the overall CWRF skills. Compared to the control CWRF, the ensemble average of these skill-enhanced physics configurations more accurately reproduces YRB summer precipitation's spatial distributions, interannual anomalies, and associated circulation patterns. The Bayesian Joint Probability calibration to these configurations improves the ensemble's spatial distributions but compromises its interannual anomalies and teleconnection patterns. Our findings highlight substantial potential for refining the representation of climate system physics to improve YRB precipitation prediction. This is notably achieved by realistically coupling cumulus, microphysics, and radiation processes to accurately capture circulation teleconnections. Further enhancements can be achieved by optimizing the multi-physics ensemble among skill-enhanced configurations.

Keywords physics parameterization, regional climate model, downscaling skill enhancement, multi-physics ensemble, teleconnection, bias reduction

1 Introduction

Summer precipitation over the Yangtze River Basin (YRB) is crucial because this region is an important economic belt in China with nearly 40% of the Chinese population and contributing over 40% of the country's total GDP (Li and Lu, 2017). Affected by highly variable East Asian summer monsoon, frequent floods and droughts observed in the YRB have caused severe socioeconomic losses (Li and Lin, 2015). Greater future risks are projected under global warming, with increasing summer precipitation and more intense and frequent

Received January 3, 2024; accepted February 20, 2024

E-mails: xliang@umd.edu (Xin-Zhong LIANG)
jhyu@nuist.edu.cn (Jinhua YU)

extremes (Zhai et al., 2005; Piao et al., 2010; Ma et al., 2015; Sun et al., 2018; Jiang et al., 2021). However, predicting YRB summer precipitation accurately remains challenging, given the intricate and complex nature of the underlying regional climate systems (Ding and Chan, 2005; Huang et al., 2012; Wang et al., 2015; Fremme and Sodemann, 2019).

General circulation models (GCMs) worldwide continue to exhibit considerable biases in simulating summer YRB precipitation, despite decades of efforts (Song and Zhou, 2014b; Kusunoki and Arakawa, 2015; Jiang et al., 2016, 2020; Xin et al., 2020). Significant underestimation of precipitation has been identified, particularly due to the absence of the major monsoon rainbands (Chen et al., 2010; Feng et al., 2014; Song and Zhou, 2014a; Chen et al., 2018). Overestimation has been shown in the Sichuan Basin, situated in the upper reach of YRB (Chen and Frauenfeld, 2014; Bao and Feng, 2016; Zhang and Chen, 2016; Li et al., 2021). Most GCMs in the recent Coupled Model Intercomparison Project phase 6 (CMIP6) still poorly simulate YRB precipitation interannual variability (Li et al., 2021). Increasing model resolution has been proposed to reduce these biases, but it cannot completely solve the problem (Kan et al., 2015; Kusunoki and Arakawa, 2015; Lin et al., 2019). Large biases remain in GCMs and regional climate models (RCMs) with grid spacing of 10−50 km (Feng et al., 2011; Bao et al., 2015; Jiang et al., 2020; Hu et al., 2021) and even in convection-permitting models at grid spacing of 4-km or less (Zhu et al., 2018; Li et al., 2020a; Yun et al., 2020). These model biases in present-day simulations may impair the reliability of climate projections, underestimating future YRB rainfall changes (Liang et al., 2008b; Chen et al., 2018; Jiang et al., 2021).

It is crucial to comprehend and rectify the fundamental physical processes responsible for errors in regional precipitation prediction. Numerous studies have focused on the sensitivity of summer precipitation prediction over east China to cumulus parameterization, exploring relationships between long-term mean biases in regional precipitation and large-scale atmospheric circulations. For instance, Bao (2013) demonstrated that the Tiedtke scheme outperforms the Grell scheme in replicating the distribution of summer monsoon precipitation, owing to its better simulation of the Western Pacific Subtropical High (WPSH) and the south-westerly low-level jet. Zhang et al. (2015) showed that the Tiedtke scheme produced smaller precipitation biases over eastern China than other three schemes, linking to its smaller errors in the East Asian summer monsoon index. Yang et al. (2015) found large impacts of the parameters in the Kain–Fritsch scheme on simulated precipitation and associated atmospheric profiles of the East Asian summer monsoon. Gui et al. (2020) demonstrated that cumulus parameterization significantly affects the summer rainfall distribution by primarily modulating biases in atmospheric circulation systems.

Interannual variations of YRB summer rainfall have also been identified with changes in large-scale systems, including the tropical western North Pacific circulation (Wang et al., 2001; Kosaka et al., 2011), the East Asian westerly jet (EAJ) (Liang and Wang, 1998; Xuan et al., 2011; Wang and Zuo, 2016), and the South Asian High (Huang and Qian, 2004; Jiang et al., 2011; Wei et al., 2015). Errors in simulating interannual anomalies of YRB summer rainfall extremes were linked to those of moisture convergence and convective available potential energy (Zhang et al., 2023). Our recent study (Zhao and Liang, 2023) demonstrated the significant potential for enhancing YRB extreme rainfall prediction by refining the physics representation in the Regional Climate-Weather Research and Forecasting model (CWRF; Liang et al., 2012). The improvement is notable by coupling appropriate cumulus, microphysics, and radiation schemes, along with optimizing the multi-physics ensemble. The enhanced performance can be primarily attributed to a more accurate representation of the EAJ and its associated regional circulation patterns.

Limited research has thus far addressed the dependence of YRB rainfall mean biases and interannual anomalies on diverse physics parameterization schemes, alongside identifying the key underlying mechanisms. Linkages of precipitation with circulation features have been studied separately in terms of mean biases and interannual anomalies. However, factors contributing to summer rainfall errors may differ from mean conditions to interannual variations or extreme events (Liang et al., 2001, 2002; Wang et al., 2011; Sun and Liang, 2020a, 2020b), requiring a systematic investigation to improve model representation across scales. Critical issues that need further investigation for YRB summer precipitation prediction include: 1) the physical processes and mechanisms causing its mean biases and interannual errors; 2) the major physics parameterizations sensitive for these biases and errors; 3) the interlinkages between model abilities in simulating mean conditions and interannual anomalies; 4) the improvements from coupling the advanced physics schemes and optimizing their multi-physics ensemble.

The multi-physics ensemble is often used to mitigate uncertainty stemming from diverse model physics representations (Liang et al., 2012). However, not all schemes excel uniformly in simulating all variables across all regions. Optimal ensemble skill can be achieved by combining the top-performing schemes, which surpasses the simple average of all available members (Jiang et al., 2015). Thus, it is desirable to select from 28 CWRF configurations (Zhao and Liang, 2023) the superior members for building an optimal ensemble to improve YRB precipitation prediction. Additionally, statistical methods have been populated to correct systematic biases (e.g., Zhang et al., 2017). Among these,

the Bayesian Joint Probability (BJP) (Wang and Robertson, 2011) method is widely used for calibrating mean climate predictions (Schepen et al., 2020). However, it is unclear whether applying the BJP calibration can also enhance the optimal ensemble prediction for interannual anomalies of YRB summer precipitation.

Therefore, the main objectives of this study are to uncover the physical mechanisms behind errors in simulating YRB summer precipitation, encompassing mean conditions and interannual anomalies, and whereby to improve prediction skills by constructing an optimal multi-physics ensemble from CWRF simulations with diverse physics representations. Our evaluation emphasizes the identification of key physical processes/mechanisms causing errors by linking them with large-scale atmospheric circulation deficiencies in both summer means and interannual variations. Rather than focusing solely on precipitation, this study incorporates a broader set of covarying circulation metrics grounded in our understanding of the underlying physical processes. Additionally, we examine whether the BJP calibration can further enhance the optimal ensemble prediction of both summer means and interannual variations.

In the following, Section 2 describes the model, experiments, observations, and methods used. Section 3 examines the impact of CWRF physics representations on YRB summer precipitation mean biases and interannual anomalies. Section 4 delves into the connections between YRB precipitation and circulation features in both mean biases and interannual anomalies, identifying the key physical mechanisms causing model errors. Section 5 identifies the superior physics configurations that best capture both precipitation characteristics and associated circulation features. Section 6 constructs the optimal multi-physics ensemble from the superior members, evaluates its consistent improvement in circulation patterns, and explores the possible enhancement by the BJP calibration. Section 7 presents the summary and conclusions.

2 Model, data, and methodology

2.1 CWRF model and experiments

CWRF, a climate extension of the Weather Research and Forecasting model (WRF; Skamarock et al., 2008), has been continuously improved in key physical processes and comprehensive system interactions among all process modules (Liang et al., 2005a, 2005b, 2012, 2019a; Choi et al., 2007, 2013; Choi and Liang, 2010; Yuan and Liang, 2011a; Xu et al., 2014; Gan et al., 2015; Ling et al., 2015; Sun et al., 2020a, 2020b; Sun and Liang, 2023). A crucial component is the incorporation of the Ensemble Cumulus Parameterization (ECP; Qiao and Liang, 2015, 2016, 2017), modified from Grell and Dévényi (2002), for simulating deep convection. Additionally, the inclusion of a Cloud-Aerosol-Radiation ensemble model (CAR) addresses intricate interactions among cloud and aerosol properties, along with radiation transfers (Liang and Zhang, 2013; Zhang et al., 2013). These enhancements contribute to CWRF's outstanding performance in reproducing seasonal to interannual precipitation and extreme statistics in both United States and China (Yuan and Liang, 2011b; Liang et al., 2012, 2019a; Chen et al., 2016; Sun and Liang, 2020a, 2020b; Li et al., 2020b; Jiang et al., 2021).

In the downscaling experiments, 28 CWRF ensemble simulations are generated using multiple physical parameterization schemes (Table S1), as outlined by Sun and Liang (2020b). This ensemble comprises one control simulation (CTL) and 27 sensitivity simulations, each of which replaces the control with an alternative scheme representing one of the six major physical processes (cumulus, microphysics, radiation, boundary layer, surface, and cloud). Comparing these ensemble simulations can facilitate our comprehensive sensitivity studies and enhance our understanding of various physical processes (Sun and Liang, 2020a).

The CWRF computational domain, as defined by Liang et al. (2019a), covers China and adjacent oceans (approximately 8°−59°N, 58°−162°E) under the Lambert conformal map projection centered at (35.18°N, 110°E), and includes 14 grids along each of the four edges within the buffer zones. The model features a horizontal grid spacing of 30 km and is equipped with 36 vertical levels extending up to 50 hPa. The lateral boundary conditions are refreshed every 6 h using data from the European Centre for Medium-Range Weather Forecasts (ECMWF) Interim Reanalysis with a grid spacing of approximately 80 km (ERI, Dee et al., 2011). All simulations are initialized on October 1, 1979 and run continuously until December 31, 2015, with the first two months dedicated to a spin-up period. Subsequently, the results from June to August (JJA) spanning the years between 1980 and 2015 are utilized for the following analysis. The YRB is defined according to Liang et al. (2019a), who devided subregions with distinct climate regimes and topographic characteristics.

2.2 Data

To evaluate the model's performance, daily precipitation observations are obtained from the CN05.1 data set, which integrates *in situ* measurements from 2416 monitoring stations and transforms them into 0.25° grids in China using objective analysis (Wu and Gao, 2013). The ERI data are employed for evaluating the CWRF downscaling skill. The latest fifth-generation reanalysis by ECMWF (ERA5, Hersbach et al., 2019), with a grid spacing of 31 km, serves as the reference proxy for

observational circulation features (Sun and Liang, 2020a, 2020b). These circulation variables include wind speed, specific humidity, and geopotential height at different pressure levels. To maintain consistency, these observational and reference data are remapped onto the CWRF 30 km grid using a conservative interpolation method.

2.3 Methodology

Section 3 assesses how physics parameterizations impact YRB's summer precipitation mean biases and interannual anomalies (from its long-term average), using measures such as bias, spatial and interannual correlation, root-mean-square-error (RMSE), and the percentage of areas in the region with significant interannual correlations (SCA). The SCA is determined by applying a density function that illustrates the frequency distribution of interannual correlations across all CWRF grids within the YRB, following Liang et al. (2019b). Section 4 employs correlation analysis to explore the relationship between YRB precipitation and associated circulation features, addressing both mean biases and interannual anomalies. This method helps identify teleconnections and define circulation and its mean bias indices for comparing the modeled and observed patterns. Section 5 ranks CWRF configurations using a comprehensive ranking measure (MR) that integrates regional precipitation and circulation indices for both mean conditions and interannual anomalies. Applying metrics individually or on specific variables may deviate the choice of good performers. Thus, we apply the precipitation-circulation covariant metrics to determine the top ranked configurations. Section 6 then develops an optimal ensemble and a BJP-calibrated ensemble from these skill-enhanced configurations, investigating model performance improvements from a climate system perspective. Our method provides a systematic examination of the model's abilities, highlighting the critical utility of the composite MR for physically based evaluation. Detailed descriptions of these methodologies can be found in the Supplementary Materials. See Appendix A for the key acronyms and abbreviations.

3 Physics dependence of YRB precipitation errors

3.1 Summer mean biases

Figure 1 compares the spatial pattern correlation (PCC), RMSE, and mean bias against observations among ERA5, ERI and 28 CWRF physics configurations in replicating the observed long-term average summer precipitation (PRA) over the YRB. Figure S1 shows the geographical distributions of PRA biases. ERI shows wet biases around 1−3 mm·day^{-1}, concentrated in the upper reach of the YRB. ERA5 improves ERI on PCC by 0.16, but features an expanded coverage of wet biases exceeding 1 mm·day^{-1}, increasing RMSE by 8%. In contrast, the CWRF CTL simulated PCC, RMSE, and bias are 0.45, 2 mm·day^{-1}, and 0.3 mm·day^{-1}, respectively. It captures the rainband with an adequate precipitation amount and a reasonable spatial pattern (Liang et al., 2019a). Compared to ERI, CWRF reduces the average wet bias by 0.4 mm·day^{-1}, but decreases PCC by 0.1 and increases RMSE by 54%.

Figure 1 illustrates that the PRA bias is largely affected by the selection of cumulus and radiation parameteriza-

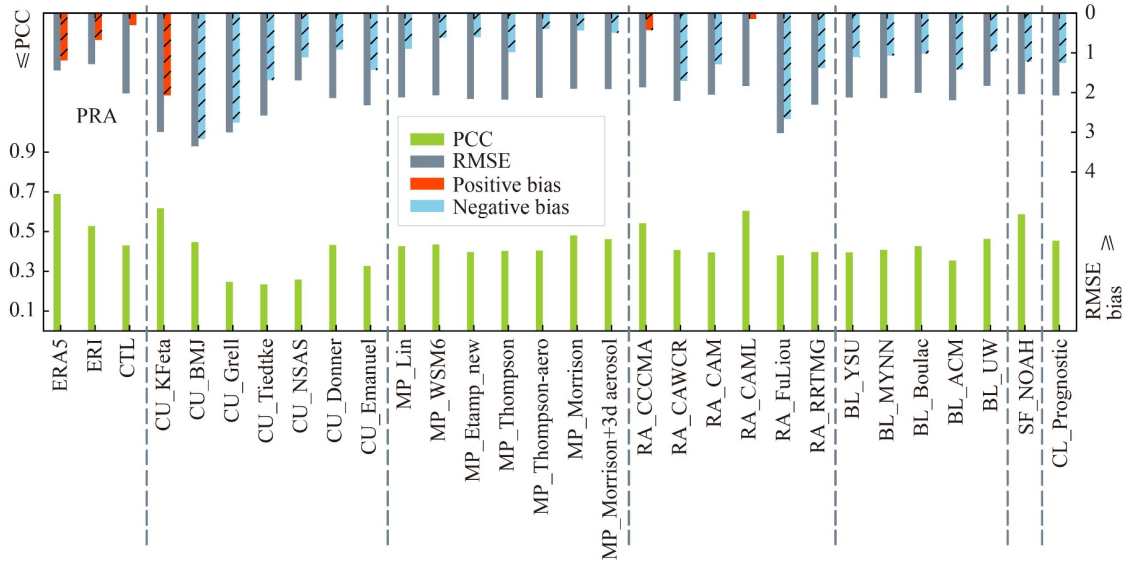

Fig. 1 The spatial pattern correlation coefficient (PCC), RMS error (RMSE), and average bias (Bias) between observations and ERA5, ERI, and 28 CWRF physics configurations for 1980−2015 mean summer precipitation (PRA, mm·day^{-1}) over the YRB. Hatches denote statistically significant differences at the 5% significance level.

tion schemes. The CTL using the ECP cumulus scheme stands out as the top performer, demonstrating a high PCC, low RMSE, and minimal wet bias among all eight cumulus schemes. KFeta produces a larger wet bias up to 6 mm·day^{-1} over extensive areas, particularly in the southern YRB (Fig. S1), increasing average bias by 1.8 mm·day^{-1} and RMSE by 50% compared to ECP. The other six cumulus schemes (BMJ, Grell, Tiedtke, NSAS, Donner, Emanuel) all generally exhibit lower PCCs around 0.23−0.33 and produce dry biases. In particular, BMJ produces the largest dry bias, exceeding 4 mm·day^{-1}, predominantly along the major rainband.

Among the six experiments with varying radiation schemes coupling ECP, the CCCMA and CAML stand out, exhibiting both adequate precipitation intensity and precise core location (Fig. S1), with only a minor wet bias (0.4 and 0.1 mm·day^{-1}) and higher PCC (0.54 and 0.60) compared to the CTL. The remaining four schemes exhibit lower PCCs than the CTL, accompanied by dry biases around 1.3−2.7 mm·day^{-1}. Additionally, the Morrison and Morrison plus 3d aerosol microphysics schemes exhibit higher PCCs (0.48 and 0.46) and smaller RMSEs than CTL, with dry biases (0.4 and 0.5 mm·day^{-1}). The NOAH surface scheme attains a higher PCC (0.59) and similar RMSE, but exhibits a more pronounced dry bias by an average of 1.2 mm·day^{-1}.

We elaborate in the Supplementary Materials on the skills concerning the number of rainy days (NRD) and daily rainfall intensity (DRI) to enhance the validity of our precipitation analysis. In summary, CWRF CTL notably mitigates the drizzle problem and more accurately depicts rainfall intensity compared to ERI, despite the latter's assimilation of surface data. Among the six major physical processes, cumulus parameterization is identified as the most influential in simulating regional climate mean precipitation characteristics. The ECP cumulus scheme in the control configuration excels in representing the main rainband, rainy days, and rainfall intensity across the YRB, especially in terms of magnitude, location, and coverage, when compared to the other seven cumulus schemes. Integrating the ECP cumulus scheme with the Morrison or Morrison plus 3d aerosol microphysics and the CCCMA or CAML radiation schemes further enhances CWRF's overall proficiency in capturing the summer mean precipitation characteristics.

3.2 Interannual anomalies

Figure 2(a) compares the geographic distributions of summer mean precipitation interannual correlations with observations during 1980−2015 among 28 different CWRF physics configurations. Figure 2(b) shows the YRB-average temporal correlation (TCC) and RMSE values, alongside the SCA values. A greater number of grids exhibiting skillful correlations, along with a larger SCA value, signifies a higher level of predictive skill.

The CTL most realistically reproduces observed precipitation interannual variations, as shown by a large coverage of SCA over 43.2% of the YRB, a basin average TCC of 0.58, and the smallest RMSE of merely 0.8 mm·day^{-1} (Fig. 2(b)). The regions displaying significant signals are mainly concentrated to the south of the middle and lower reaches of the Yangtze River, while the regions with limited skills are between the Yellow and Yangtze Rivers (Fig. 2(a)).

Interannual variation errors also display notable sensitivity to the parameterization schemes. Among the eight cumulus schemes, KFeta distinguishes itself with a 37.1% higher SCA and a larger TCC of 0.70 compared to CTL, but its RMSE is substantially higher by 206%. Other cumulus schemes generally show much smaller SCAs around 11%−42% of the YRB, lower TCCs in 0.18−0.55, and larger RMSEs between 1.3 and 3.1 mm·day^{-1}. The BMJ, Grell, Tiedtke, and Emanuel schemes even have insignificant TCCs.

Among the six radiation schemes, both CCCMA and CAML exhibit excellent predictive skills in interannual variation, showcasing comparable higher SCAs and TCCs to KFeta, along with similar lower RMSEs compared to CTL. The Morrison and Morrison plus 3d aerosol microphysics schemes slightly elevate TCCs, albeit somewhat reducing SCAs and increasing RMSEs compared to CTL.

The above results affirm the major impact of cumulus parameterization on regional precipitation simulation for both summer mean conditions and interannual anomalies, followed by radiation and microphysics parameterizations. The CWRF control configuration integrating the ECP cumulus scheme, along with the Morrison or Morrison plus 3d aerosol microphysics and the CCCMA or CAML radiation schemes, excels in simulating YRB precipition's summer mean distribution and also demonstrates a robust ability to capture its interannual variation.

4 Mechanisms causing YRB precipitation errors

Figure 3 presents the summer mean geographic distributions of the observed precipitation and ERA5 circulation characteristics, including 200-hPa zonal wind (U200), 850-hPa meridional wind (V850), total precipitable water (TPW), and 200-hPa geopotential height (H200). Figure 4 illustrates the teleconnection patterns between the long-term mean biases in CWRF simulated YRB-average summer precipitation and those in point-wise key circulation features. Figure 5 further shows the observed teleconnection patterns between interannual anomalies of the YRB-average summer monthly precipitation and those of the ERA5 circulation distributions. We assume individual model independence for the correlations

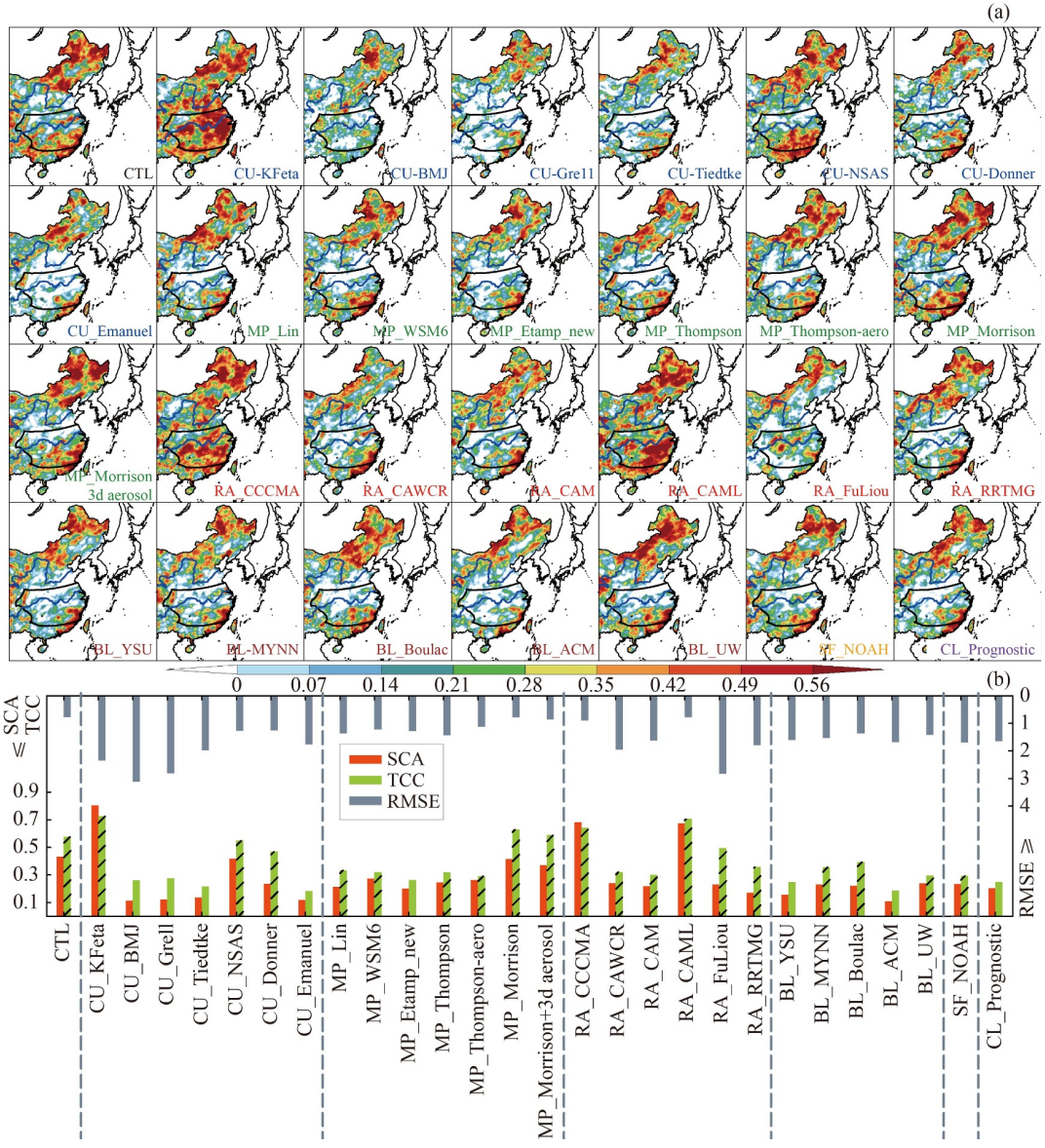

Fig. 2 (a) Geographic distributions of 1980−2015 summer precipitation interannual correlations between observations and 28 CWRF physics configurations. (b) YRB-average temporal correlation coefficient (TCC) and RMS error (RMSE, mm·day^{-1}), and the percentage of areas in the YRB that have significant interannual correlations (SCA × 100, %). Correlations exceeding 0.28 as column hatched denote the 5% significance level under the one-tail Student's *t*-test. The YRB region is enclosed by the thick black outline.

among mean biases (Fig. 4) and monthly independence for the observed patterns (Fig. 5). Below we identify the physical processes and underlying mechanisms causing biases and linking anomalies.

The YRB is located to the right of the exit region of the strong westerly jet stream, with the core centered over Xinjiang (Fig. 3(a)). Significant positive correlations between precipitation and U200 biases among ERI and 28 CWRF physics configurations are situated along the jet exit, while significant negative correlations are concentrated over north-east China (Fig. 4(a)). Corresponding to a positive precipitation bias in the YRB is a positive westerly wind bias along the jet exit. A similar pattern is found in the relationship between observed interannual variations (Fig. 5(a)), with the center of significant positive correlations extending southward into the northern part of the YRB. A positive precipitation anomaly in the YRB is associated with the southward shift of the westerly jet stream, which is consistent with previous studies (Liang and Wang, 1998). The southward movement of the westerly jet stream induces the ascending branch of the jet-induced vertical circulation situated in the YRB, resulting in increased summer precipitation over there (e.g., Xuan et al., 2011). Furthermore, significant negative correlations between precipitation and U200 biases are evident over the Indian Ocean, the South China Sea, and the western Pacific (Fig. 4(a)). This pattern also corresponds well to the observed

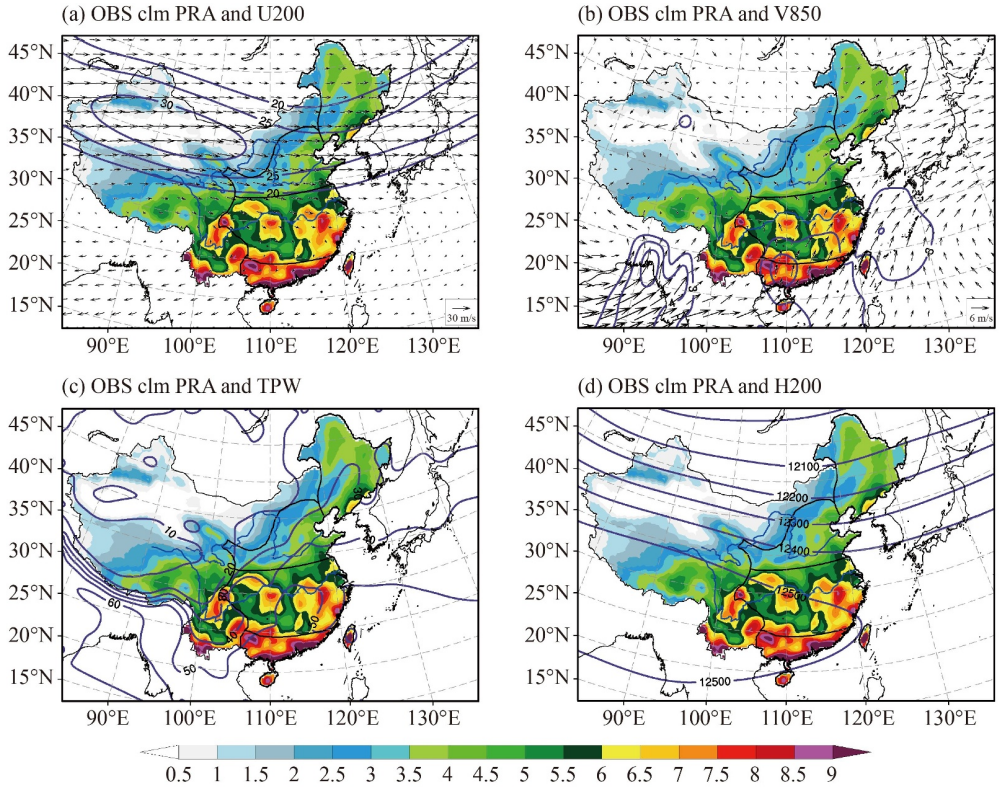

Fig. 3 Geographic distributions of 1980–2015 mean observed summer precipitation (PRA, mm·day^{-1}), overlaid with ERA5 (a) 200-hPa wind vectors and zonal wind (U200, contours at 5 m·s^{-1} intervals starting from 20), (b) 850-hPa wind vectors and meridional wind (V850, contours at 1 m·s^{-1} intervals starting from 3), (c) total precipitable water (TPW, 10 mm contour intervals), and (d) 200-hPa geopotential height (H200, 100 gpm contour intervals).

interannual variation relationships (Fig. 5(a)), implying that enhanced precipitation over the YRB is linked to a weakened Hadley circulation (Wang et al., 2011). Hence, a model placing EAJ to the south of observations and producing a weaker Hadley circulation is prone to generating increased YRB precipitation (Liang et al., 2001).

Two low-level southerly wind branches from the Bay of Bengal and South China Sea-western Pacific, transport moisture across southern and eastern China (Fig. 3(b)), leading to great moisture flux convergence south of the Yangtze River (Fig. 3(c)). Significant positive correlations between YRB precipitation and V850 biases exist over south China and the South China Sea (Fig. 4(b)), closely matching the observed interannual variation relationship (Fig. 5(b)). Stronger southerly flow over south China and the South China Sea associates with a westward extension of the Subtropical high (Wang et al., 2011; Zhao et al., 2015). Increased YRB precipitation is also concurrent with a reinforced northerly flow to the north of the YRB, as evidenced by the negative correlation with V850 biases in the northern YRB (Fig. 4(b)). Meanwhile, significant positive correlations are found between YRB precipitation and local TPW in both simulated mean biases and observed interannual variations (Figs. 4(c) and 5(c)), which can be attributed to the increased low-level tropospheric convergence and intensified upward motion within the YRB (Wang et al., 2011; Li and Lu, 2017). Additionally, significant negative correlations exist between observed precipitation and TPW situated over the South China Sea-the western Pacific (Fig. 5(c)). This indicates a weakened Hadley circulation, coupled with the westward expansion or intensification of the subtropical high (Kosaka et al., 2011; Wang et al., 2011). Therefore, a model featuring a stronger southerly flow to the south of the YRB or northerly flow to the north of the YRB, along with elevated TPW, is prone to producing increased YRB precipitation.

The South Asian High (SAH), represented by the 12500-gpm contour at 200 hPa, covers the southern YRB and south China (Fig. 3(d)). Significant positive correlations between YRB precipitation and H200 biases centered over South Tibet and encompass a broad region, while significant negative correlations are present remotely across north-east China and North Korea (Fig. 4(d)). This teleconnection pattern closely mirrors the observed interannual variation relationships (Fig. 5(d)), despite significant positive correlations are evident over the subtropical South Asian continent. This indicates that an anomalous south-eastward shift of SAH, often accompanied by an intensified westward-stretching subtro-

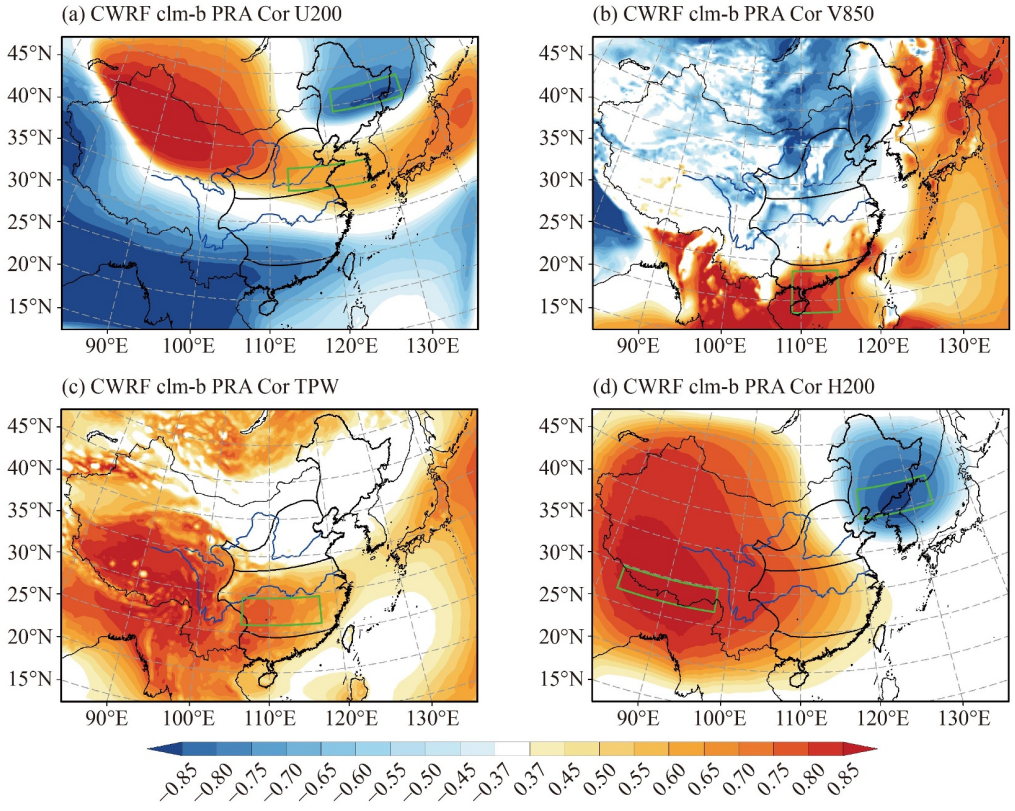

Fig. 4 Spatial distribution of correlations between long-term mean YRB-average summer precipitation biases (from observations) among ERI and 28 CWRF physics configurations, and their pointwise circulation departures (from ERA5) for (a) U200, (b) V850, (c) TPW, and (d) H200. Colored areas indicate statistically significant correlations at the 5% significance level, assuming individual model independence. The outlined regions with statistically significant high (positive or negative) correlations are defined as the core correlation areas, which are used to compute the circulation bias indices.

pical high, promotes increased rainfall over the YRB (Jiang et al., 2011; Wei et al., 2015; Ning et al., 2017). Thus, a model with SAH biased south-east of the observations is likely to generate increased YRB precipitation.

Clearly, significant correlations exist between the bias in YRB precipitation and that in atmospheric circulation. The fundamental features of the model mean bias teleconnections and the observed interannual variation relationships are highly consistent, indicating that simulated precipitation biases are linked to errors in atmospheric circulation predictions. When the EAJ is biased to the south, the intensity of both low-level southerly winds to the south of the YRB and the northerly winds to the north of the YRB are overpredicted, accompanied by the SAH south-eastward movement and overestimated precipitable water within the YRB, the YRB precipitation tends to enhance.

To evaluate how well the model simulates associated key circulations in both summer means and interannual variations, we employ corresponding circulation indices (refer to the Supplementary Materials for details). Note that minor shifts in the centers of these teleconnection patterns would not notably impact the defined indices, given the extensive coverage of significant correlations (Liang et al., 2008a).

Figure 6 depicts scattering relationships between the YRB regional mean summer precipitation biases (from observations) and the circulation departures (from ERA5 analyses) averaged over their respective teleconnected areas outlined in Fig. 4. These relationships are compared among ERI and 28 CWRF physics configurations. The model spread in precipitation biases is primarily determined by deviations in these circulation features of U200, V850, TPW, and H200. These factors account for 53%, 69%, 52%, and 84% of the variance in precipitation biases, respectively. Moreover, ERI realistically captures circulation features, while CWRF CTL generates slightly larger biases, ranging from (0.2 $m \cdot s^{-1}$, −0.4 $m \cdot s^{-1}$, 0.8 mm, −0.3 gpm) to (−3.0 $m \cdot s^{-1}$, 0.8 $m \cdot s^{-1}$, −4.7 mm, −28.4 gpm). This surpasses the common anticipation for models to closely replicate these variables at a skill level comparable to ERI, which assimilates comprehensive data to accurately capture interactions among precipitation, land, and atmospheric processes (Liang et al., 2019a).

The CWRF's ability to replicate the key observed circulation features varies significantly among different physics configurations. The variation is most pronounced among eight cumulus and seven radiation parameteriza-

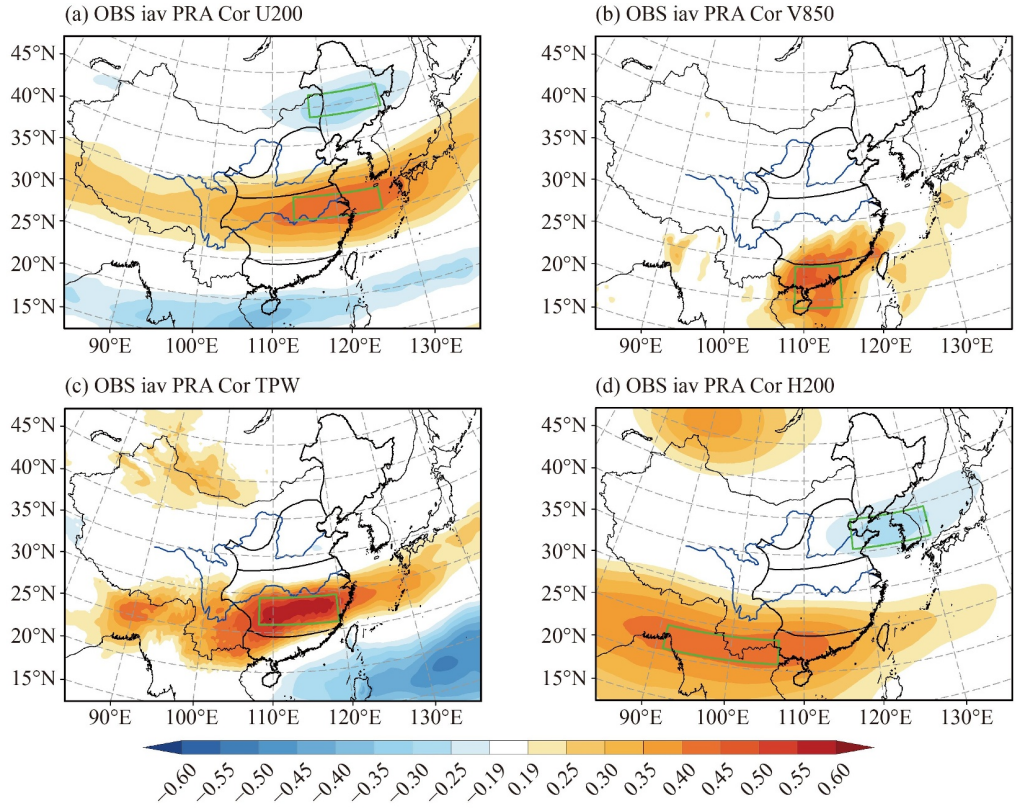

Fig. 5 Spatial distribution of correlations between the interannual anomalies of the observed YRB-average summer monthly precipitation and those of the ERA5 pointwise circulation for (a) U200, (b) V850, (c) TPW, and (d) H200. Colored areas denote statistically significant correlations at the 5% significance level, assuming monthly independence. The outlined regions with statistically significant high (positive or negative) correlations are defined as the core correlation areas, which are used to compute the circulation indices.

tions, covering a notably wide range of deviations such as 12 m/s for U200, 3 m/s for V850, 9 mm for TPW, and 136 gpm for H200. In contrast, the variations in circulation departures among different microphysics, boundary layer, surface, and cloud schemes are less pronounced, with deviations of only 8 m/s, 1 m/s, 4 mm, and 70 gpm for U200, V850, TPW, and H200, respectively.

Figure 7 presents the interannual correlations between summer monthly precipitation anomalies averaged over the YRB and anomalies in the circulation features averaged over the observed teleconnected area outlined in Fig. 5. The correlations are compared among observations, ERI, and CWRF simulations using 28 physics configurations. Correlation coefficient exceeding 0.19 is deemed statistically significant at the 5% significant level. Significant positive correlations with observed circulation features range from 0.38 (H200), 0.42 (U200), 0.44 (V850) to 0.63 (TPW), underscoring the considerable impact of these circulation variations on YRB summer precipitation (Fig. 5). Compared to the observed interannual variation relationships, ERI generally exhibits weaker correlations, ranging from 0.25 (U200), 0.38 (V850), 0.42 (TPW) to 0.23 (H200). However, CWRF CTL more accurately replicates the observed relationships, with correlations of 0.51 (U200), 0.48 (V850), 0.72 (TPW), and 0.47 (H200), respectively. As such, CWRF downscaling holds promise for incorporating enhanced representations of physical processes to capture the interannual variation of regional precipitation and associated circulation characteristics.

For U200 (Fig. 7(a)), CWRF physics configurations consistently yield significant positive correlations, except for the BMJ cumulus and Fuliou radiation schemes. Note that 22 out of the 28 configurations simulate the correlations close to the observed 0.42, deviating by 0.1 and averaging around 0.45. For V850 (Fig. 7(b)), the majority of configurations reveal significant positive correlations, apart from the BMJ cumulus scheme. Only 17 among the 28 configurations simulate the correlations near the observed 0.44, deviating by 0.1 and averaging 0.41. For both TPW and H200 (Figs. 7(c) and 7(d)), all configurations show significant positive correlations. Among them, 25 configurations generate the TPW correlations matching the observed 0.63, with a deviation of 0.1 and an average around 0.67. Likewise, 20 configurations demonstrate the H200 correlations that align closely with the observed 0.38, deviating by 0.1 and averaging around 0.42. In summary, CWRF demonstrates superior performance in simulating the relationship between summer precipitation anomalies in the YRB and

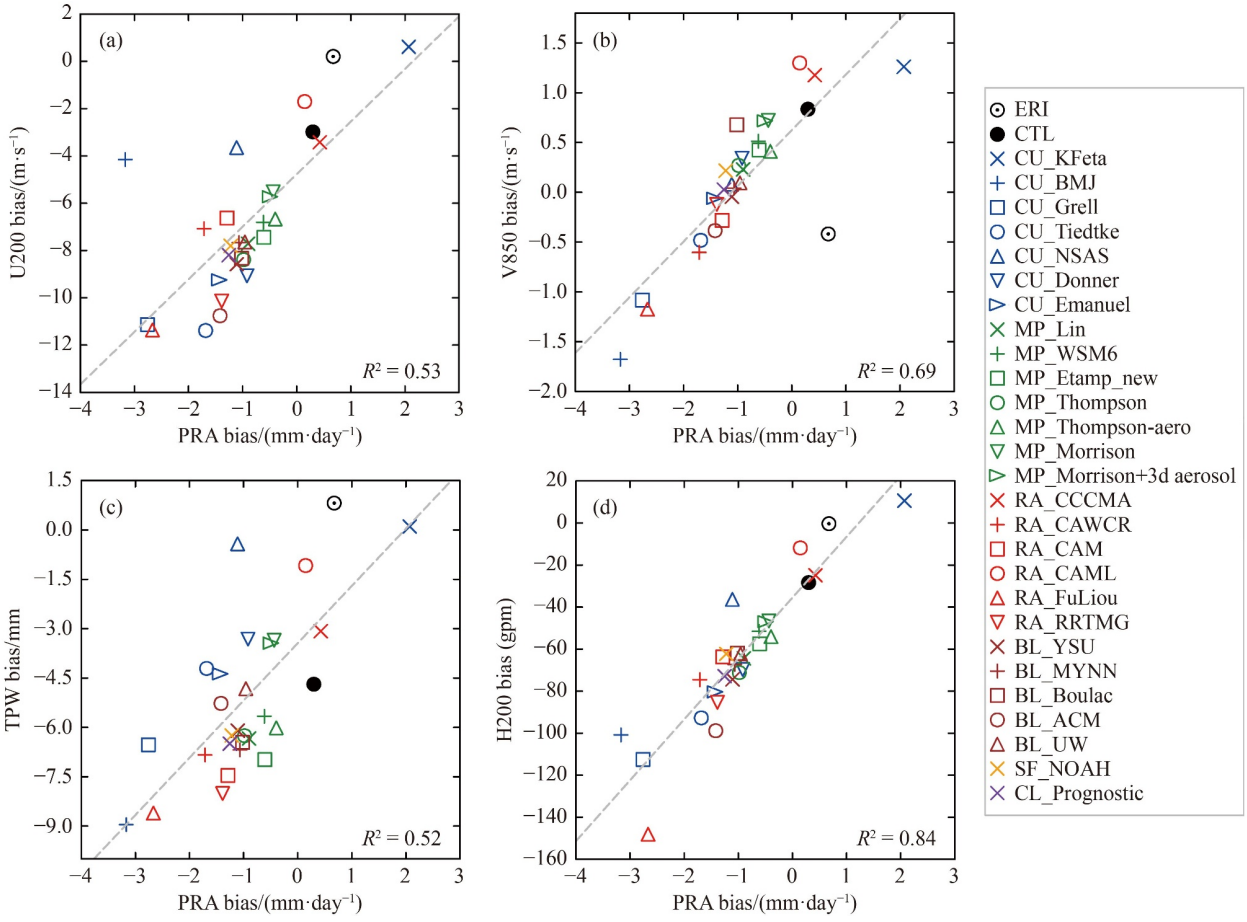

Fig. 6 Scatterplots of the YRB-average summer precipitation biases (from observations) and the circulation departures (from ERA5 analyses) for (a) U200, (b) V850, (c) TPW, and (d) H200 averaged over the respective teleconnected areas specified in Fig. 4 for both ERI and 28 CWRF physics configurations. Also marked is the explained variance (R^2).

large-scale circulation features. Most of its physics configurations effectively capture observed interannual variation relationships with U200, TPW and H200, having some exceptions with V850.

5 System coupling among precipitation and circulation deficiencies

Independent analyses have been conducted on the mechanisms of mean precipitation biases and interannual errors as in our previous sections. This section employs precipitation-circulation covariant metrics to quantify interconnections among these model deficiencies. Focusing on models with high performance, we further diagnose the physical processes underlying the YRB precipitation mean biases and interannual errors. Figure 8 compares the models' MR rankings for simulating summer mean YRB precipitation and its key circulation features (U200, V850, TPW, H200), against their rankings in representing interannual variations. The strong correlation of 0.70, surpassing the 5% significance level, highlights the models' proficiency in simultaneously representing both the mean conditions and interannual variations of YRB regional precipitation and related circulation dynamics.

The rankings vary significantly across different models. ERI ranks higher for mean conditions of precipitation and circulation (0.83) compared to interannual variations (0.53). This occurs because ERI uses data assimilation to constrain precipitation variation, weakening the circulation control. In contrast, CWRF CTL demonstrates more balanced high MR values, scoring 0.67 and 0.62 for mean conditions and interannual variations, respectively. Among all eight cumulus schemes, the ECP scheme emerges as the overall best performer in capturing both regional precipitation and circulation features, achieving the most balanced and highest MR values for summer means and interannual variations. While NSAS ranks slightly higher than ECP for mean conditions (0.68), but ranks significantly lower for interannual variations (0.55). This leads to reduced interannual agreement in precipitation and circulations, corresponding to larger dry biases (see Figs. 1 and 2). Other cumulus schemes perform considerably worse than ECP, particularly BMJ, Grell, and Tiedtke rank the lowest with MR values

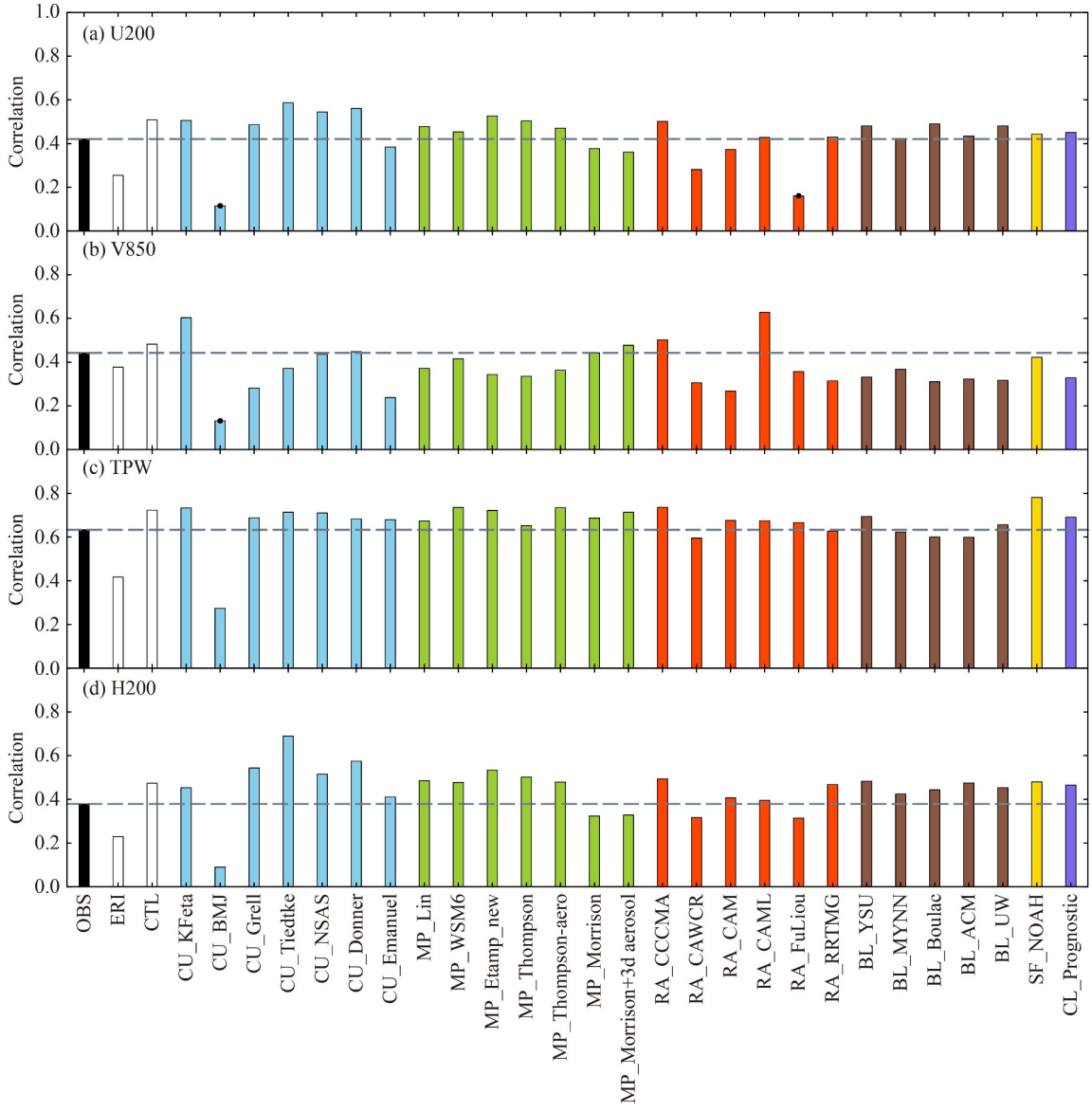

Fig. 7 Correlations between the interannual anomalies of the YRB-average summer monthly precipitation and those of circulation features for (a) U200, (b) V850, (c) TPW, and (d) H200, averaged over the observed teleconnected area depicted in Fig. 5. The correlations are presented for observations, ERI and 28 CWRF physics configurations, distinguished by colors based on their underlying physical processes. Black circles indicate correlations that are not statistically significant at the 5% significance level, and horizontal lines depict the observed values.

consistently below 0.23.

Coupling the ECP cumulus scheme with the Morrison or Morrison plus 3d aerosol microphysics scheme and the CCCMA or CAML radiation scheme enhances the CWRF's ability to replicate observed regional precipitation and associated circulation features, resulting in MR values of 0.67 and 0.58 for mean conditions and interannual variations, respectively.

Focusing solely on smaller mean biases, the five top-ranked configurations are using the CTL, CAML, and CCCMA radiation, the Thompson-aero and Morrison microphysics schemes (Fig. 1). Whereas focusing on higher interannual correlations (TCC), the leading configurations are the KFeta cumulus, Morrison and Morrison plus 3d aero microphysics, and CAML and CCCMA radiation schemes (Fig. 2). This solo approach, however, lacks stability and does not effectively link precipitation and circulation biases or errors, as seen with schemes like the KFeta cumulus scheme (Fig. 8). To overcome the problem, we adopt a composite MR method, combining multiple metrics {precipitation, circulation, and both} for {mean bias, interannual anomaly, and both}. This method consistently identifies the same five top-ranked configurations: using the CTL, the Morrison and Morrison plus 3d aerosol microphysics, and the CCCMA and CAML radiation schemes (Figs. 8

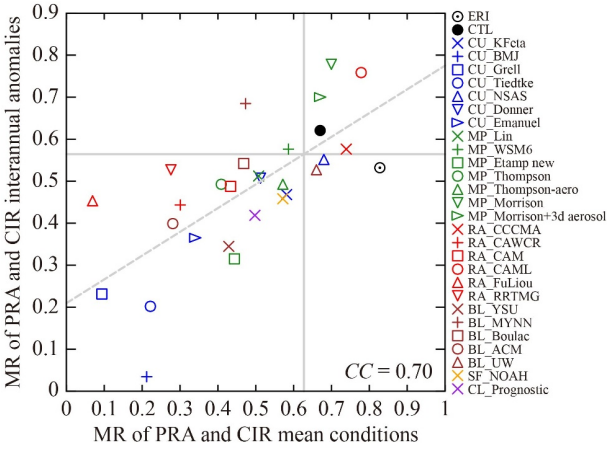

Fig. 8 Scatter diagram showing models' MR of simulated summer mean YRB precipitation and associated circulation features (U200, V850, TPW, H200) (*x*-axis) and that of interannual variations (*y*-axis). Also marked is the correlation coefficient (CC). Models positioned in the top-right quadrant demonstrate commendable performance across both criteria.

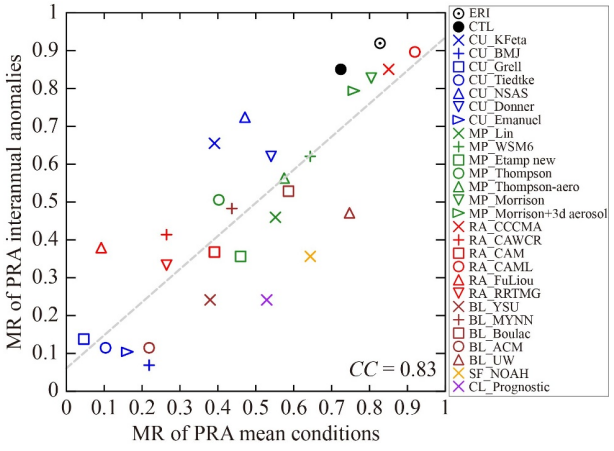

Fig. 9 Scatter diagram showing models' MR of simulated YRB summer precipitation mean conditions and interannual anomalies. Also marked is the correlation coefficient (CC).

and 9). Such consistency confirms the coherence of the precipitation system simulation and the objective ranking based on the composite MR. These results highlight the pivotal role of the system coupling, especially among cumulus, radiation and microphysics processes in predicting not only YRB extreme precipitation (Zhao and Liang, 2023) but also mean precipitation and interannual variations.

Figures 10 and 11 compare the geographic distributions of 36-year mean summer circulation characteristics, encompassing 200/850 hPa wind, 200/500 hPa geopotential height, column moisture flux, and precipitation, among ERA5, ERI, and the five top-ranked CWRF configurations, using the CTL, Morrison and Morrison plus 3d aerosol microphysics, and the CCCMA and CAML radiation schemes. Compared to ERA5, ERI shows a slight northward shift and a pronounced eastward expansion of SAH (see Supplementary Materials for the definition of its index), extending its eastern boundary over the Pacific, and shrinks the EAJ exit westward toward Hebei (Fig. 10), both contributing to weakened upward motions and decreased precipitation across a wide span from North to South China (Fig. S1). As discussed in more detail below, the general SAH northward shift and the underestimation of the EAJ exit intensity in the CWRF simulations may originate from ERI forcing errors.

CWRF CTL, compared to ERA5, exhibits a noticeable westward displacement in SAH's eastern sector, along with a northward shift similar to that of ERI (Fig. 10). This weakens the westerlies on SAH's north side, underestimating EAJ by approximately 3 m/s in southern North China and northern YRB and slightly displacing the jet axis northward with its exit extended westward toward Hebei. Consequently, upward motions increase directly beneath the EAJ exit and over south China but decrease in the southern YRB. Collectively, these adjustments contribute to WPSH's northward shift, leading to intensified low-level south-westerly winds that transport more moisture to the upper reaches of the Yangtze and Pearl Rivers, with less moisture reaching near the coast (Fig. 11). Thus, CWRF CTL alleviates ERA5's wet biases in the YRB, but exacerbates them in north and south China (Fig. S1).

Compared to CTL, the EAJ exit in both the Morrison and Morrison plus 3d aerosol microphysics schemes experiences a more pronounced westward displacement toward Shanxi, resulting in larger EAJ underestimations exceeding 4 m/s in southern north China and northern YRB regions. This shift, along with a more realistic presence of low-level southerlies over eastern China, contributes to larger underestimations of moisture convergence across an expanded YRB region. Collectively, these factors lead to weakened ascending motions and decreased rainfall in north China and YRB, while enhanced ascending motions and rainfall in south China. As a result, these schemes reduce wet biases in north China compared to CTL, but exacerbate them in south China and introduce small dry biases in the YRB. Overall, the Morrison scheme demonstrates smaller circulation biases compared to its combination with the 3d aerosol effect, thereby providing a more accurate portrayal of regional precipitation patterns.

The CCCMA radiation scheme produces a northward shift of SAH, similar to CTL, with an eastward extension toward the coast. The EAJ exit is displaced westward to Shanxi, accompanied by a larger underestimation of approximate 4 m/s in southern north China. Consequently, upward motions are weakened in north China but strengthened in the southern YRB and south China, compared to CWRF CTL. Intensified low-level south-westerlies over southern YRB and south China also

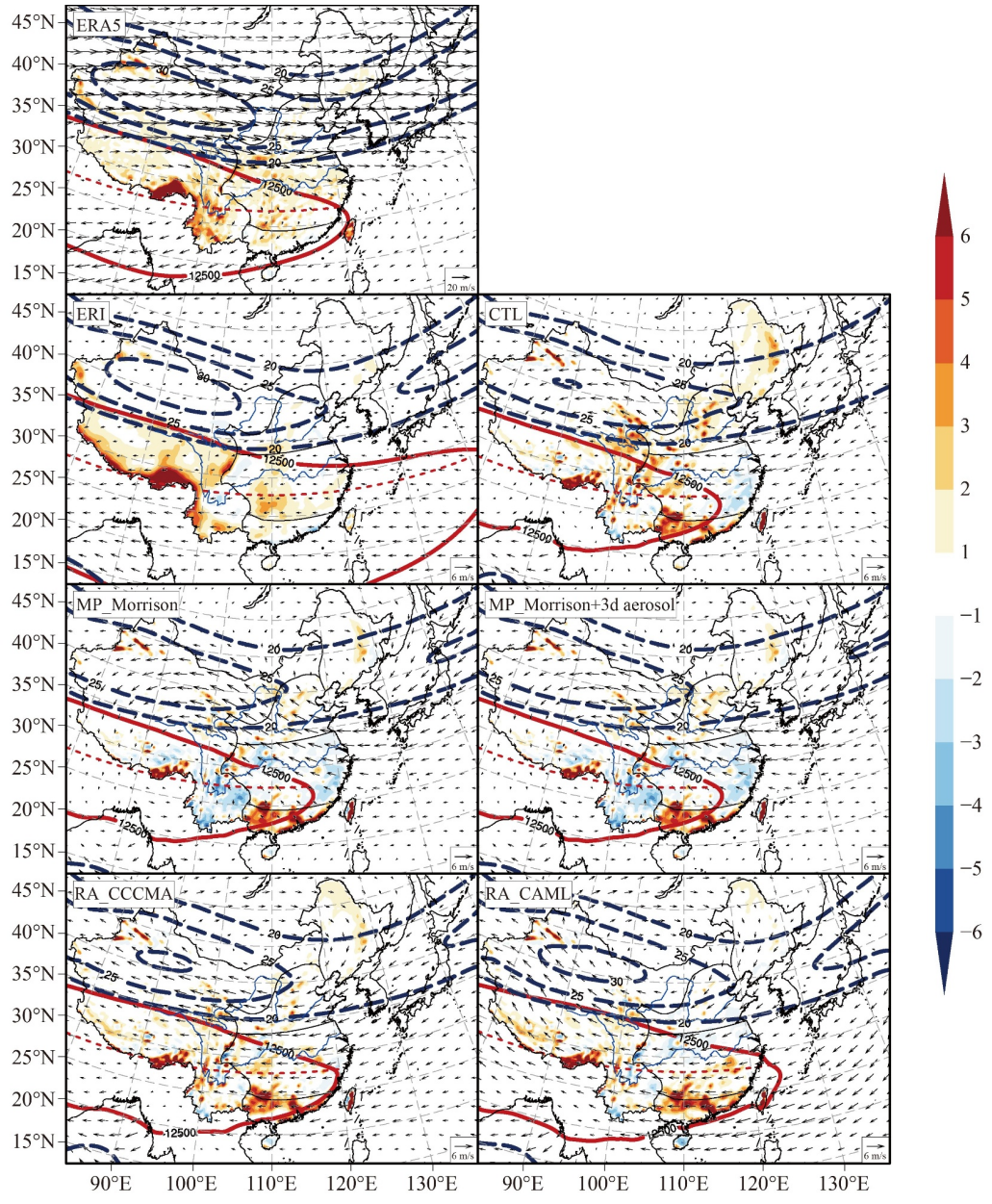

Fig. 10 1980−2015 mean summer wind at 200 hPa ($m \cdot s^{-1}$, vectors) based on ERA5 and their departures from ERA5 as indicated by ERI and five CWRF physics configurations. Overlaid are the corresponding precipitation biases (from observations, color shadings), 200-hPa wind speeds ($m \cdot s^{-1}$, dashed contours starting from 20 at intervals of 5), and 200-hPa geopotential height represented by solid contour at 12,500 gpm with its ridge (red dash contour).

promote stronger moisture flux convergence to the south of the Yangtze River but suppress it to the north. As a result, when compared to CTL, the CCCMA radiation scheme reduces wet biases in north China but simultaneously amplifies them in the YRB and south China.

The CAML radiation scheme simulates a similar northward shift of SAH, expanding its ridge to cover a larger portion of south-eastern China, with a weaker EAJ extending its exit eastward toward Hebei. This leads to weakened ascending motions north of the Yangtze River but largely enhanced them south of the River. The eastward shift of WPSH and the low-level south-westerlies, accompanied with north-easterly flow perturbations in north China and north of the Yangtze River, weakens moisture fluxes in these regions but intensifies them in south China. Consequently, compared to CTL, the CAML scheme reduces wet biases in the YRB but increases them in south China, with small dry biases in north China.

Therefore, summer mean biases in YRB precipitation are strongly associated with those in large-scale atmospheric circulations. The wet biases simulated by CWRF CTL, and those by using the CCCMA and CAML radiation schemes, are linked to a subtle SAH northward

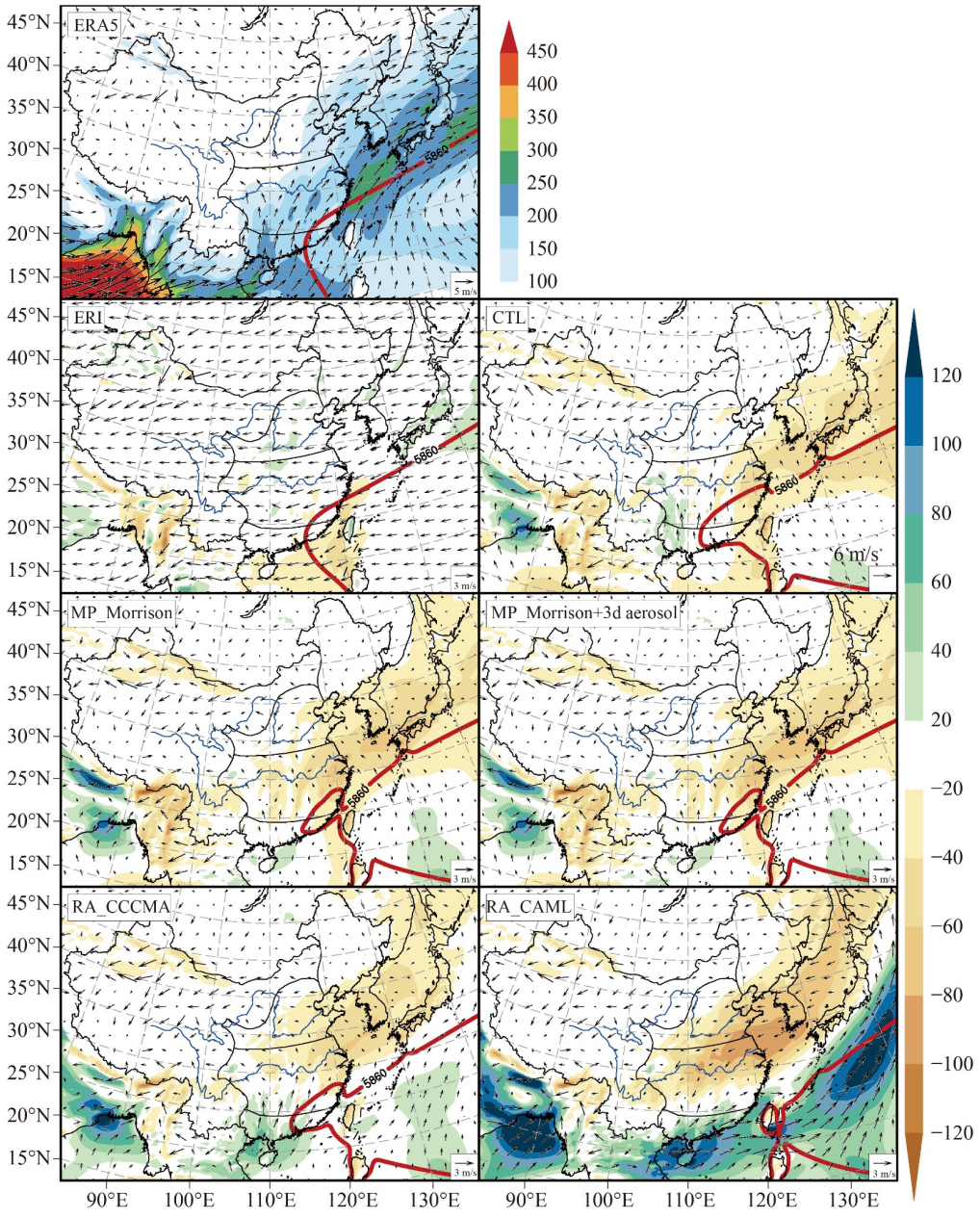

Fig. 11 1980–2015 mean summer wind at 850 hPa ($m \cdot s^{-1}$, vectors) and vertically integrated (1000–300 hPa) moisture flux ($kg \cdot m^{-1} \cdot s^{-1}$, color shadings) based on ERA5 and their departures from ERA5 as indicated by ERI and five CWRF physics configurations. Overlaid are the corresponding 500-hPa geopotential height represented by solid contour at 5860 gpm.

shift and a slight EAJ weakening, which enhances the low-level southerly wind and its moisture transport into the YRB. Conversely, the dry biases simulated by the Morrison and Morrison plus 3d aerosol microphysics schemes are associated with a more significantly weakened EAJ, leading to reduced moisture transport into the YRB.

Figure 12 compares the teleconnection patterns between summer monthly precipitation interannual anomalies in the YRB and large-scale circulation features among ERI and the five top-ranked CWRF physics configurations. Relative to the observed U200 correlations (Fig. 5(a)), ERI struggles to replicate the pattern by producing much weaker correlation cores that are excessively biased toward the south (Fig. 12(a)). In contrast, CWRF CTL more effectively captures these cores, exhibiting a well-distributed and magnified pattern. The Morrison and Morrison plus 3d aerosol microphysics and CAML radiation schemes generally show weaker correlations. Conversely, the CCCMA radiation scheme exhibits higher correlation magnitudes compared to CTL.

For V850 correlations (Fig. 5(b)), all models generally match the observed core location but vary in magnitude (Fig. 12(b)). ERI produces lower correlations, whereas

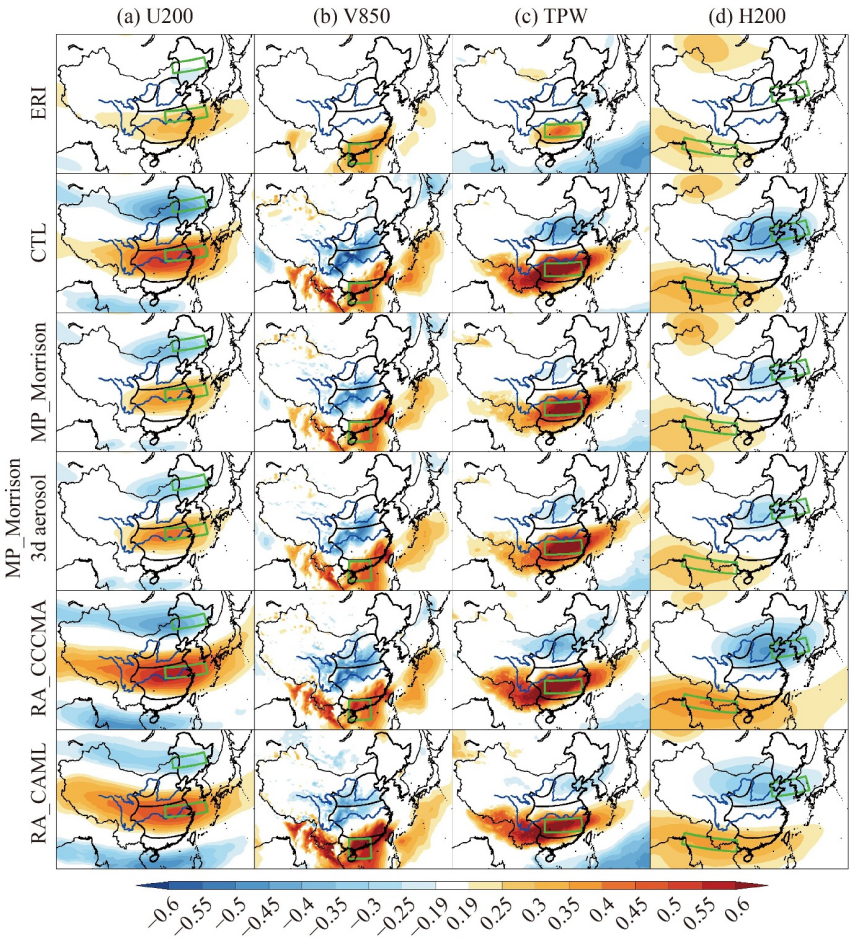

Fig. 12 Same as Fig. 5 except for interannual correlations of ERI and five CWRF physics configurations.

CWRF CTL exhibits higher correlations. The Morrison and Morrison plus 3d aerosol microphysics and CCCMA radiation schemes achieve similar correlation magnitudes as CTL, comparable to observations. In contrast, the CAML radiation scheme simulates higher correlations than CTL. For TPW correlations (Fig. 5(c)), ERI shrinks the core area with lower correlations, whereas CWRF CTL expands it with higher correlations (Fig. 12(c)). All the five top-ranked physics schemes perform comparably to CTL.

For H200 correlations (Fig. 5(d)), ERI shifts the positive core to the north-west of observations and misses the negative core with much lower magnitudes (Fig. 12(d)). CWRF CTL outperforms ERI by better capturing both positive and negative core areas with realistic magnitudes. The Morrison and Morrison plus 3d aerosol microphysics schemes produce negative correlations weaker than CTL but close to observed values, while they both exhibit significantly lower positive correlations. In contrast, the CCCMA and CAML radiation schemes improve over CTL with realistically higher positive correlations, while CAML also better captures the negative correlations.

Therefore, CWRF CTL outperforms ERI in capturing more accurate interannual teleconnection patterns, both in magnitude and spatial distribution. Incorporating the ECP cumulus scheme with the Morrison or Morrison plus 3d aerosol microphysics and CCCMA or CAML radiation schemes enhances CWRF's overall ability to capture the observed circulation teleconnection for YRB precipitation interannual anomalies.

6 Multi-physics ensemble to improve YRB precipitation prediction

Figure 13(a) compares the geographic distributions of summer mean precipitation among ERA5, ERI, CWRF CTL and its best multi-physics ensemble (BMPE). The BMPE is defined as the average of the five top-ranked CWRF physics configurations. Also shown are the spatial pattern correlation, RMSE, and mean bias over the YRB compared to observations. The observed major rainband exhibits peak values exceeding 7 mm·day^{-1} along the Yangtze River, particularly in the upper and lower reaches (Fig. 3). ERA5 produces excessive precipitation, surpassing 8 mm·day^{-1} over more extensive areas along the Yangtze River. This leads to a high pattern correlation

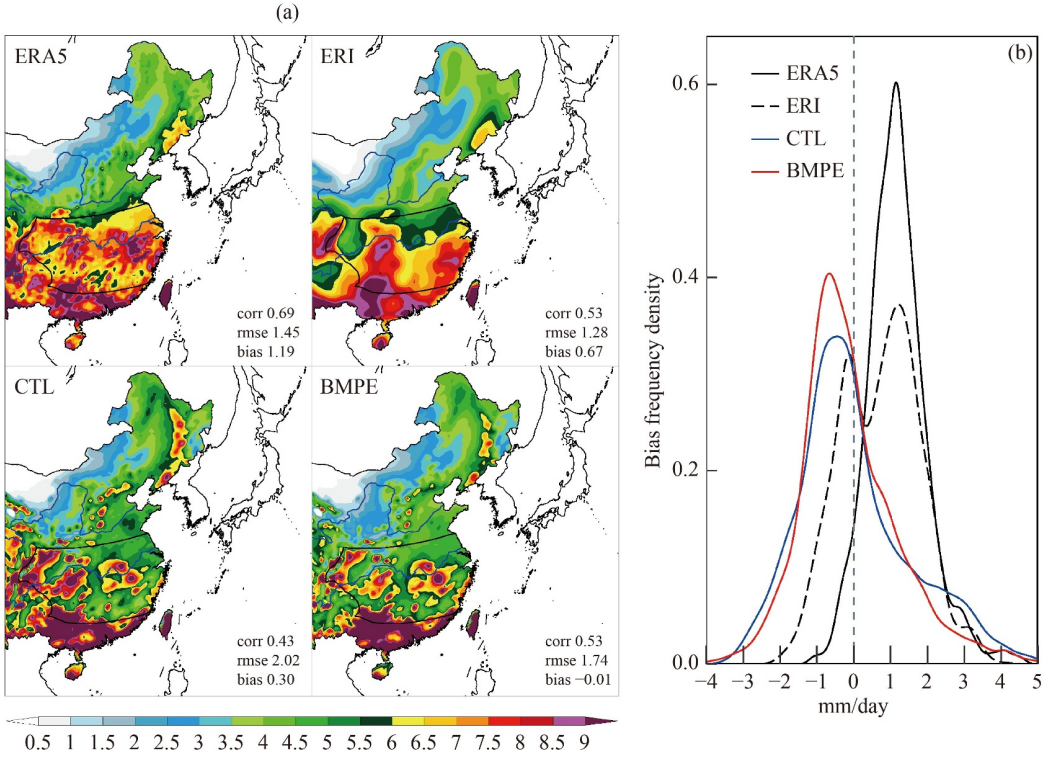

Fig. 13 (a) Spatial distributions of summer average precipitation as assimilated (ERA5 and ERI), CWRF control (CTL) and the best multi-physics ensemble (BMPE). Listed with the corresponding spatial pattern correlation, RMS error (rmse) and bias over the YRB compared with observations. (b) bias frequency density distributions over the YRB.

(0.69) but a larger RMSE (1.5 mm·day^{-1}), with a systematic wet bias of 1.2 mm·day^{-1} averaged over the YRB. ERI also produces intensive precipitation, exceeding 7.5 mm·day^{-1} in the upper reach of the River and along the south-east coast. This results in a lower correlation (0.53), a smaller RMSE (1.3 mm·day^{-1}) and an average wet bias of 0.7 mm·day^{-1}. While CWRF CTL captures the primary rainband's features with an average wet bias reduced to 0.3 mm·day^{-1}, but has a lower correlation (0.43) and a larger RMSE (2.0 mm·day^{-1}). Importantly, BMPE enhances CTL skills systematically, showing a higher correlation (0.53), a reduced RMSE (1.7 mm·day^{-1}), and a minimum average dry bias of 0.01 mm·day^{-1}.

Figure 13(b) compares precipitation bias frequency distributions at all grids within the YRB among ERA5, ERI, and CWRF CTL and BMPE. ERA5 exhibits a prominent peak at a bias of 1.2 mm·day^{-1}, indicating an overall overestimation. ERI displays a structure of double peaks at biases of 1.3 and −0.1 mm·day^{-1}, with frequent occurrences of both overestimates and underestimates. CWRF CTL shows a peak near −0.5 mm·day^{-1}, with frequent small underestimates, accompanied by a flatter distribution. BMPE resembles CTL in the distribution pattern but exhibits a sharper peak around −0.7 mm·day^{-1}.

Figures 14(a) and 14(b) compare the geographic distributions of summer precipitation interannual correlations with observations during 1980−2015 simulated by CWRF CTL and BMPE, as well as their frequency distributions for all grids within the YRB and respective SCAs. CWRF CTL captures observed interannual anomalies over 43.2% area of the YRB, with two frequency peaks at the correlations of 0.21 and 0.34. Different from the summer mean simulation, BMPE significantly enhances the CTL skill of interannual variation, with the frequency peak shifting to the correlation of 0.36 and the area of significant correlations expanding to 69.7%, primarily in the southern region of the Yangtze River. Figure 14(c) compares YRB-average summer precipitation interannual anomalies observed and simulated by CWRF CTL and BMPE. Clearly, BMPE elevates the CTL skill, enhancing the interannual anomaly correlation by 0.13 and reducing RMSE by 27%.

Figure 15 depicts BMPE summer mean circulations. BMPE successfully reproduces SAH, WPSH, and the low-level southerlies over eastern China, but shifts the EAJ exit westward to Shanxi. This shift underestimates the EAJ streak by 3 m/s across southern north China and northern YRB and weakens ascending motions there, while enhancing them across southern YRB and south China. As such, BMPE simulates smaller (than CTL) moisture fluxes into the YRB. Consequently, BMPE simultaneously improves north China by reducing wet biases and the YRB with negligible dry biases, albeit south China remains too wet. The improvements made in BMPE stem from the cancellation of errors across its

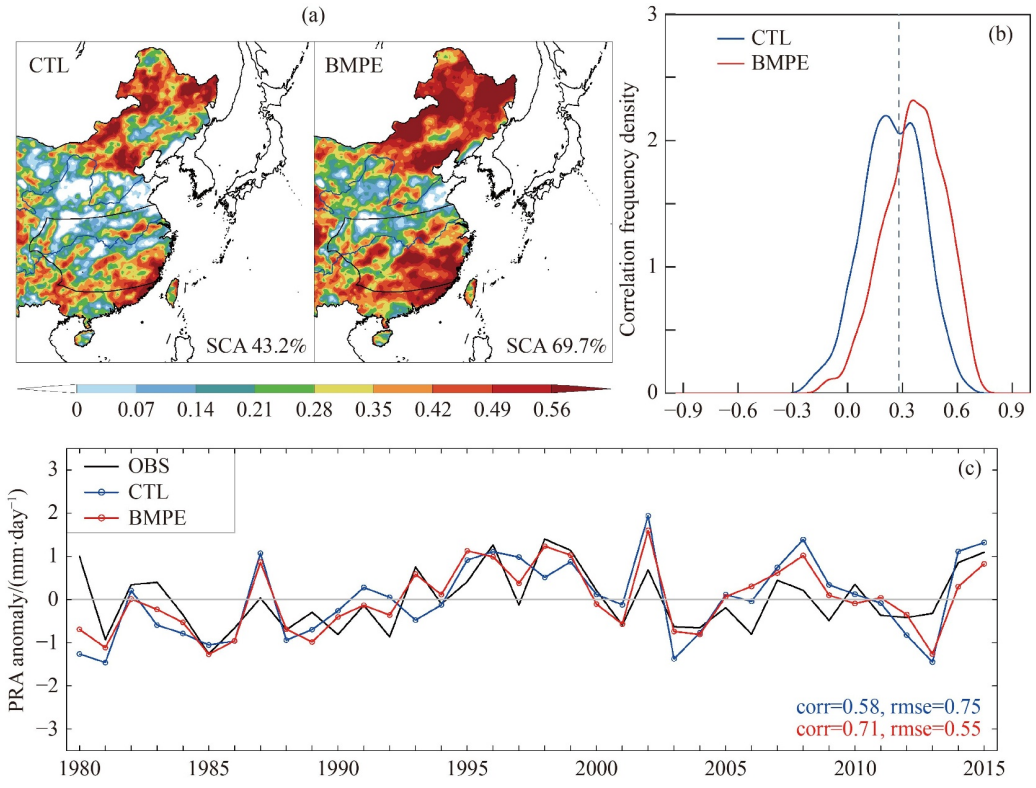

Fig. 14 CWRF CTL and BMPE simulated (a) interannual correlations of summer precipitation with observations, along with the percentage of basin areas that have significant interannual correlations (SCA). (b) frequency density functions of correlations at all CWRF grids within the YRB. Correlations above 0.28 marked by the vertical line are statistically significant at the 5% significance level, determined by a one-tail Student's *t*-test. (c) YRB-average precipitation interannual anomalies, along with their interannual correlation (corr) and RMS error (rmse) against observations.

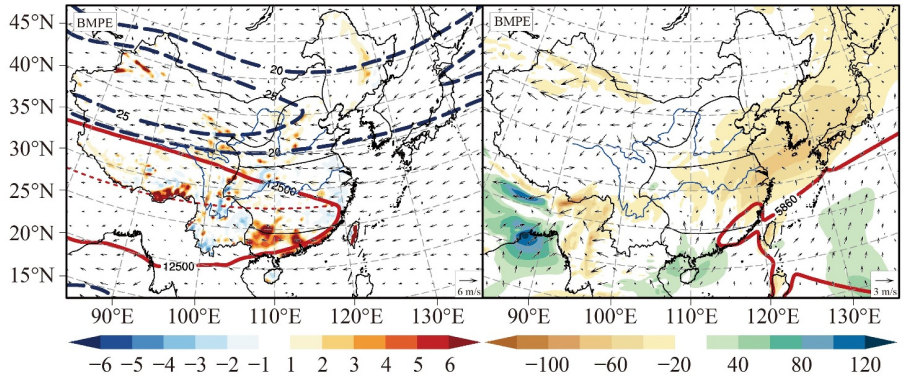

Fig. 15 CWRF BMPE simulated (left) summer mean 200-hPa wind (m·s^{-1}, vectors) departures from ERA5, overlaid with precipitation biases (color shadings), 200-hPa wind speeds (m·s^{-1}, dashed contours starting from 20 at intervals of 5), and 200-hPa geopotential height (solid contour at 12500 gpm with ridge as red dash contour). (right) 850-hPa wind (m·s^{-1}, vectors) and vertically integrated (1000−300 hPa) moisture flux (kg·m^{-1}·s^{-1}, color shadings) departures from ERA5, overlaid with the 500-hPa geopotential height represented by solid contour at 5860 gpm.

member configurations.

Additionally, the BJP method is applied to correct biases in the individual members of BMPE and then construct a new ensemble mean BMPE_bjp. As compared in detail in the Supplementary Materials, BMPE_bjp, by design, substantially improves BMPE for mean conditions. However, BMPE_bjp performs notably worse than BMPE in predicting interannual variations of YRB precipitation and associated circulations. Thus, the BJP calibration reduces the BMPE advantage to represent interannual anomalies and teleconnection patterns. To this end, BMPE, simply averaging the high-performing multi-physics configurations, significantly enhances the prediction of both mean conditions and interannual anomalies.

7 Summary and conclusions

This study aims to understand the fundamental physical mechanisms responsible for the mean biases and interannual errors in simulating YRB summer precipitation, and develop a multi-physics ensemble from the top-performed CWRF configurations that best represent these mechanisms to improve the prediction. We first analyze the dependence of these precipitation biases and errors on 28 configurations of varying physics parameterization schemes. The analysis focuses on teleconnections in long-term mean biases between YRB precipitation and large-scale circulations including 200-hPa zonal wind (U200), 850-hPa meridional wind (V850), total precipitable water (TPW), and 200-hPa geopotential height (H200). We also analyze the observed correlation patterns of interannual anomalies between YRB summer monthly precipitation and the corresponding circulations. We then define a distinct set of the circulation indices based on the dominant action centers in these simulated mean bias teleconnections and observed interannual correlation patterns. These distinct indices form the precipitation-circulation covariant metrics for both summer means and interannual variations. Finally, we use a comprehensive ranking measure (MR) from the covariant metrics to identify the superior configurations and construct the best multi-physics ensemble (BMPE). Our key findings can be summarized as follows.

First, CWRF control configuration (CTL) excels over ERI in capturing summer mean rainband and rainfall intensity and effectively addressing the drizzling problem, even though ERI assimilates surface data. Cumulus parameterization has the largest impact on the YRB precipitation simulation, followed by radiation and microphysics parameterizations. Especially, the ensemble cumulus parameterization (ECP) used in CTL outperforms other seven cumulus schemes in CWRF for both summer precipitation mean conditions and interannual anomalies. When coupling with ECP, the Morrison or Morrison plus 3d aerosol microphysics and the CCCMA or CAML radiation schemes enhance the overall CWRF skills.

Second, model mean biases in YRB precipitation are teleconnected with those in large-scale circulations. Significant correlations include U200 positive centers along the jet exit and negative centers in north-east China, V850 positive centers over south China and the South China Sea, TPW positive centers over the YRB, and H200 positive centers over South Tibet and negative centers across north-east China and North Korea. These simulated bias teleconnections are consistent with the observed correlation patterns of interannual anomalies between YRB summer monthly precipitation and the corresponding circulations. Despite minor changes in their primary action centers, this alignment implies that the underlying physical processes for the observed interannual anomalies are also responsible for the relationships among model biases. Specifically, YRB precipitation is enhanced by a southward shift of the East Asian westerly jet (EAJ), a south-eastward displacement of the South Asian High (SAH), a strengthening of low-level southerlies to the south of the YRB, and an increase of moisture influx into the YRB. Conversely, reduced YRB precipitation is associated with an opposite circulation pattern.

Third, our developed covariant metrics and MR measure objectively quantify models' overall performance in consistently capturing mean conditions and interannual variations of YRB summer precipitation and its associated large-scale circulations. The integration of the ECP cumulus scheme with the Morrison or Morrison plus 3d aerosol microphysics and the CCCMA or CAML radiation schemes enhances the CWRF ability in predicting YRB precipitation and its circulation teleconnection characteristics. These five physics configurations constitute the top performers. CWRF CTL and its ECP members coupling the CCCMA and CAML radiation schemes simulate a slightly northward shifted SAH and a mildly weakened EAJ, leading to increased upward motions in the YRB. They also produce intensified low-level south-westerlies with larger moisture transport, causing wet biases in the YRB. In contrast, the ECP members coupling the Morrison and Morrison plus 3d aerosol microphysics schemes simulate a moderately weakened EAJ and decreased upward motions with less moisture transport, causing dry biases in the YRB.

Fourth, BMPE of the five top-ranked configurations significantly enhances the CWRF ability in capturing summer YRB precipitation and circulation teleconnection in both mean distributions and interannual variations. Compared to CTL, BMPE more faithfully reproduces the associated circulations such as the SAH and WPSH. It simulates a slightly attenuated EAJ, decreasing upward motions in the north and increasing them in the south of the YRB. It also generates a decreased moisture flux into the YRB, resulting in minor dry biases. As expected, Bayesian Joint Probability calibrations to the BMPE members notably reduce the ensemble's overall mean biases, but unfortunately worsen the skills in predicting interannual anomalies and teleconnection patterns.

In conclusion, this study develops a unique set of precipitation-circulation covariant metrics to quantify the physical linkages between YRB precipitation and its associated circulations for both mean conditions and interannual variations, and use these metrics to systematically determine models' precipitation errors and contributing factors. The approach provides an objective way to identify the top-skilled and physically consistent model configurations. It also guides the formation of the best multi-physics ensemble that maximizes the CWRF ability to predict YRB precipitation seasonal-interannual characteristics. Effectively coupling model representations of cumulus, microphysics, and radiation processes

stands as the pivotal linchpin for accurately capturing YRB precipitation and its influential dynamic climate system.

Acknowledgments This research was funded by the US National Science Foundation Innovations at the Nexus of Food, Energy and Water Systems (US-China INFEWS) under Grant EAR1903249, the China Meteorological Administration/National Climate Center research subcontract 2211011816501, and the the Shanghai 2021 "Scientific and technological innovation action plan" Natural Science Foundation (Grant No. 21ZR1420400). The authors thank the Computational and Information Systems Laboratory of the National Center for Atmospheric Research, the ECNU Multifunctional Platform for Innovation 001 facilities and the Wuxi National Supercomputing Center for their support in terms of CWRF simulations and analyses. We would like to express our sincere gratitude to Chief Editor Dr. Wei Gao for the prompt handling of the review process; his efficiency greatly facilitated the publication of our work. We also thank the anonymous reviewers for their constructive comments and suggestions, which significantly improved the presentation of our manuscript.

Supplementary material is available in the online version of this article at https://doi.org/10.1007/s11707-024-1118-x and is accessible for authorized users.

Competing Interests The authors declare that they have no competing interests.

Author Contributions Conceptualization, Y.Z. and X.L.; methodology, Y.Z. and X.L.; software, Y.Z.; validation, Y.Z.; investigation, Y.Z.; resources, X.L.; data curation, Y.Z.; writing—original draft preparation, Y.Z; writing—review and editing, F.Q., X.L. and J.Y.; supervision, X.L. All authors have read and agreed to the published version of the manuscript.

Data Availability All CWRF experiment simulations used to generate the analysis results in the manuscript are available from the corresponding author upon request. Observational data and analysis results used in this study are accessible online (please email authors for website address).

Appendix A Acronyms and abbreviations

BJP	Bayesian Joint Probability
BMPE	Best multi-physics ensemble
BMPE_bjp	Ensemble of BJP calibrations applied to the individual BMPE members
CWRF	Climate-weather research and forecasting model
CTL	Control simulation
DRI	Daily rainfall intensity
EAJ	East Asian westerly jet
ECP	Ensemble cumulus parameterization
ERI	European Centre for Medium-Range Weather Forecasts interim reanalysis
ERA5	European Centre for Medium-Range Weather Forecasts fifth-generation reanalysis
H200	200-hPa geopotential height
MR	Comprehensive ranking measure
NRD	Number of rainy days
PRA	Average precipitation
SAH	South Asian High
SCA	Percentage of areas in the region with significant interannual correlations
TPW	Total precipitable water
U200	200-hPa zonal wind
V850	850-hPa meridional wind
WPSH	Western Pacific Subtropical High
YRB	Yangtze River Basin

References

Bao J, Feng J (2016). Intercomparison of CMIP5 simulations of summer precipitation, evaporation, and water vapor transport over Yellow and Yangtze River basins. Theor Appl Climatol, 123(3–4): 437–452

Bao J, Feng J, Wang Y (2015). Dynamical downscaling simulation and future projection of precipitation over China. J Geophys Res Atmos, 120(16): 8227–8243

Bao Y (2013). Simulations of summer monsoon climate over East Asia with a Regional Climate Model (RegCM) using Tiedtke convective parameterization scheme (CPS). Atmos Res, 134: 35–44

Chen H, Zhou T, Neale R B, Wu X, Zhang G J (2010). Performance of the new NCAR CAM3.5 in East Asian summer monsoon simulations: sensitivity to modifications of the convection scheme. J Clim, 23(13): 3657–3675

Chen L, Frauenfeld O W (2014). A comprehensive evaluation of precipitation simulations over China based on CMIP5 multimodel ensemble projections. J Geophys Res Atmos, 119(10): 5767–5786

Chen L, Liang X Z, DeWitt D, Samel A N, Wang J X (2016). Simulation of seasonal US precipitation and temperature by the nested CWRF-ECHAM system. Clim Dyn, 46(3–4): 879–896

Chen X, Wu P, Roberts M J, Zhou T (2018). Potential underestimation of future mei-yu rainfall with coarse-resolution climate models. J Clim, 31(17): 6711–6727

Choi H I, Kumar P, Liang X Z (2007). Three-dimensional volume-averaged soil moisture transport model with a scalable parameterization of subgrid topographic variability. Water Resour Res, 43(4): W04414

Choi H I, Liang X Z (2010). Improved terrestrial hydrologic representation in mesoscale land surface models. J Hydrometeorol, 11(3): 797–809

Choi H I, Liang X Z, Kumar P (2013). A conjunctive surface–subsurface flow representation for mesoscale land surface models. J Hydrometeorol, 14(5): 1421–1442

Dee D P, Uppala S M, Simmons A J, Berrisford P, Poli P, Kobayashi S, Andrae U, Balmaseda M A, Balsamo G, Bauer P, Bechtold P, Beljaars A C M, van de Berg L, Bidlot J, Bormann N, Delsol C, Dragani R, Fuentes M, Geer A J, Haimberger L, Healy S B, Hersbach H, Hólm E V, Isaksen L, Kållberg P, Köhler M, Matricardi M, McNally A P, Monge-Sanz B M, Morcrette J J, Park B K, Peubey C, de Rosnay P, Tavolato C, Thépaut J N, Vitart F (2011). The ERA-Interim reanalysis: configuration and performance of the data assimilation system. Q J R Meteorol Soc, 137(656): 553–597

Ding Y, Chan J C (2005). The East Asian summer monsoon: an overview. Meteorol Atmos Phys, 89(1–4): 117–142

Feng J, Wei T, Dong W, Wu Q, Wang Y (2014). CMIP5/AMIP GCM simulations of East Asian summer monsoon. Adv Atmos Sci, 31(4): 836–850

Feng L, Zhou T, Wu B, Li T, Luo J J (2011). Projection of future precipitation change over China with a high-resolution global atmospheric model. Adv Atmos Sci, 28(2): 464–476

Fremme A, Sodemann H (2019). The role of land and ocean evaporation on the variability of precipitation in the Yangtze River valley. Hydrol Earth Syst Sci, 23(6): 2525–2540

Gan Y, Liang X Z, Duan Q, Choi H I, Dai Y, Wu H (2015). Stepwise sensitivity analysis from qualitative to quantitative: application to the terrestrial hydrological modeling of a Conjunctive Surface-Subsurface Process (CSSP) land surface model. J Adv Model Earth Syst, 7(2): 648–669

Grell G, Dévényi D (2002). A generalized approach to parameterizing convection combining ensemble and data assimilation. Geophys Res Lett, 29(14): 38–41

Gui S, Yang R, Cao J, Huang W (2020). Precipitation over East Asia simulated by ECHAM6.3 with different schemes of cumulus convective parameterization. Clim Dyn, 54(9–10): 4233–4261

Hersbach H, Bell B, Berrisford P, Horányi A, Sabater J M, Nicolas J, Radu R, Schepers D, Simmons A, Soci C (2019). Global reanalysis: goodbye ERA-Interim, hello ERA5. ECMWF Newsl, 159: 17–24

Hu Y, Ha Y, Zhong Z, Sun Y, Zhu Y (2021). Interdecadal variation of biases in a regional climate model simulation of summer climate of East Asia. Int J Climatol, 41(S1): E26–E38

Huang R, Chen J, Wang L, Lin Z (2012). Characteristics, processes, and causes of the spatio-temporal variabilities of the East Asian monsoon system. Adv Atmos Sci, 29(5): 910–942

Huang Y, Qian Y (2004). Relationship between South Asian high and characteristic of precipitation in mid-and lower-reaches of Yangtze River and North China. Plateau Meteorol, 23: 68–74

Jiang D, Hu D, Tian Z, Lang X (2020). Differences between CMIP6 and CMIP5 models in simulating climate over China and the East Asian monsoon. Adv Atmos Sci, 37(10): 1102–1118

Jiang D, Tian Z, Lang X (2016). Reliability of climate models for China through the IPCC Third to Fifth Assessment Reports. Int J Climatol, 36(3): 1114–1133

Jiang R, Sun L, Sun C, Liang X Z (2021). CWRF downscaling and understanding of China precipitation projections. Clim Dyn, 57(3–4): 1079–1096

Jiang X, Li Y, Yang S, Wu R (2011). Interannual and interdecadal variations of the South Asian and western Pacific subtropical highs and their relationships with Asian-Pacific summer climate. Meteorol Atmos Phys, 113(3–4): 171–180

Jiang Z, Li W, Xu J, Li L (2015). Extreme precipitation indices over China in CMIP5 models. Part I: model evaluation. J Clim, 28(21): 8603–8619

Kan M, Huang A, Zhao Y, Zhou Y, Yang B, Wu H (2015). Evaluation of the summer precipitation over China simulated by BCC_CSM model with different horizontal resolutions during the recent half century. J Geophys Res Atmos, 120(10): 4657–4670

Kosaka Y, Xie S P, Nakamura H (2011). Dynamics of interannual variability in summer precipitation over East Asia. J Clim, 24(20): 5435–5453

Kusunoki S, Arakawa O (2015). Are CMIP5 models better than CMIP3 models in simulating precipitation over East Asia? J Clim, 28(14): 5601–5621

Li F, Lin Z (2015). Improving multi-model ensemble probabilistic prediction of Yangtze River valley summer rainfall. Adv Atmos Sci, 32(4): 497–504

Li P, Furtado K, Zhou T, Chen H, Li J, Guo Z, Xiao C (2020a). The diurnal cycle of East Asian summer monsoon precipitation simulated by the Met Office Unified Model at convection-permitting scales. Clim Dyn, 55(1–2): 131–151

Li Q, Wang T, Wang F, Liang X Z, Zhao C, Dong L, Zhao C, Xie B (2020b). Dynamical downscaling simulation of the East Asian summer monsoon in a regional Climate-Weather Research and Forecasting model. Int J Climatol, 41: E1700–E1716

Li X, Lu R (2017). Extratropical factors affecting the variability in summer precipitation over the Yangtze River basin, China. J Clim, 30(20): 8357–8374

Li Y, Yan D, Peng H, Xiao S (2021). Evaluation of precipitation in CMIP6 over the Yangtze River Basin. Atmos Res, 253: 105406

Liang X Z, Choi H I, Kunkel K E, Dai Y, Joseph E, Wang J X, Kumar P (2005a). Surface boundary conditions for mesoscale regional climate models. Earth Interact, 9(18): 1–28

Liang X Z, Kunkel K E, Meehl G A, Jones R G, Wang J X (2008b). Regional climate models downscaling analysis of general circulation models present climate biases propagation into future change projections. Geophys Res Lett, 35(8): L08709

Liang X Z, Li Q, Mei H, Zeng M (2019b). Multi-grid nesting ability to represent convections across the gray zone. J Adv Model Earth Syst, 11(12): 4352–4376

Liang X Z, Samel A N, Wang W C (2002). China's rainfall interannual predictability: dependence on the annual cycle and surface anomalies. J Clim, 15(17): 2555–2561

Liang X Z, Sun C, Zheng X, Dai Y, Xu M, Choi H I, Ling T, Qiao F, Kong X, Bi X, Song L, Wang F (2019a). CWRF performance at downscaling China climate characteristics. Clim Dyn, 52(3): 2159–2184

Liang X Z, Wang W C (1998). Associations between China monsoon rainfall and tropospheric jets. Q J R Meteorol Soc, 124(552): 2597–2623

Liang X Z, Wang W C, Samel A (2001). Biases in AMIP model simulations of the east China monsoon system. Clim Dyn, 17(4): 291–304

Liang X Z, Xu M, Gao W, Kunkel K, Slusser J, Dai Y, Min Q, Houser P R, Rodell M, Schaaf C B, Gao F (2005b). Development of land surface albedo parameterization based on Moderate Resolution Imaging Spectroradiometer (MODIS) data. J Geophys Res, 110: D11107

Liang X Z, Xu M, Yuan X, Ling T, Choi H, Zhang F, Chen L, Liu S, Su S, Qiao F, He Y, Wang J, Kunkel K, Gao W, Joseph E, Morris V, Yu T W, Dudhia J, Michalakes J (2012). Regional Climate-Weather Research and Forecasting Model (CWRF). Bull Am Meteorol Soc, 93(9): 1363–1387

Liang X Z, Zhang F (2013). The cloud–aerosol–radiation (CAR)

ensemble modeling system. Atmos Chem Phys, 13(16): 8335–8364

Liang X Z, Zhu J, Kunkel K E, Ting M, Wang J X (2008a). Do CGCMs simulate the North American monsoon precipitation seasonal–interannual variability? J Clim, 21(17): 4424–4448

Lin L, Gettelman A, Xu Y, Wu C, Wang Z, Rosenbloom N, Bates S C, Dong W (2019). CAM6 simulation of mean and extreme precipitation over Asia: sensitivity to upgraded physical parameterizations and higher horizontal resolution. Geosci Model Dev, 12(8): 3773–3793

Ling T, Xu M, Liang X Z, Wang J X, Noh Y (2015). A multilevel ocean mixed layer model resolving the diurnal cycle: development and validation. J Adv Model Earth Syst, 7(4): 1680–1692

Ma S, Zhou T, Dai A, Han Z (2015). Observed changes in the distributions of daily precipitation frequency and amount over China from 1960 to 2013. J Clim, 28(17): 6960–6978

Ning L, Liu J, Wang B (2017). How does the South Asian High influence extreme precipitation over eastern China? J Geophys Res Atmos, 122(8): 4281–4298

Piao S, Ciais P, Huang Y, Shen Z, Peng S, Li J, Zhou L, Liu H, Ma Y, Ding Y, Friedlingstein P, Liu C, Tan K, Yu Y, Zhang T, Fang J (2010). The impacts of climate change on water resources and agriculture in China. Nature, 467(7311): 43–51

Qiao F, Liang X Z (2015). Effects of cumulus parameterizations on predictions of summer flood in the Central United States. Clim Dyn, 45(3–4): 727–744

Qiao F, Liang X Z (2016). Effects of cumulus parameterization closures on simulations of summer precipitation over the United States coastal oceans. J Adv Model Earth Syst, 8(2): 764–785

Qiao F, Liang X Z (2017). Effects of cumulus parameterization closures on simulations of summer precipitation over the continental United States. Clim Dyn, 49(1–2): 225–247

Schepen A, Everingham Y, Wang Q J (2020). On the joint calibration of multivariate seasonal climate forecasts from GCMs. Mon Weather Rev, 148: 437–456

Skamarock W C, Klemp J B, Dudhia J, Gill D O, Barker D M, Wang W, Powers J G (2008). A description of the Advanced Research WRF version 3. Tech Rep.

Song F, Zhou T (2014a). The climatology and interannual variability of East Asian summer monsoon in CMIP5 coupled models: does air–sea coupling improve the simulations? J Clim, 27(23): 8761–8777

Song F, Zhou T (2014b). Interannual variability of East Asian Summer Monsoon simulated by CMIP3 and CMIP5 AGCMs: skill dependence on Indian Ocean–Western Pacific anticyclone teleconnection. J Clim, 27(4): 1679–1697

Sun C, Liang X Z (2020a). Improving US extreme precipitation simulation: dependence on cumulus parameterization and underlying mechanism. Clim Dyn, 55(5–6): 1325–1352

Sun C, Liang X Z (2020b). Improving US extreme precipitation simulation: sensitivity to physics parameterizations. Clim Dyn, 54(11–12): 4891–4918

Sun C, Liang X Z (2023). Understanding and reducing warm and dry summer biases in the Central United States: improving cumulus parameterization. J Clim, 36(7): 2015–2034

Sun H, Wang A, Zhai J, Huang J, Wang Y, Wen S, Zeng X, Su B (2018). Impacts of global warming of 1.5 C and 2.0 C on precipitation patterns in China by regional climate model (COSMO-CLM). Atmos Res, 203: 83–94

Sun L, Liang X Z, Ling T, Xu M, Lee X (2020a). Improving a multilevel turbulence closure model for a shallow lake in comparison with other 1-D models. J Adv Model Earth Syst, 12: e2019MS001971

Sun L, Liang X-Z, Xia M (2020b). Developing the coupled CWRF-FVCOM modeling system to understand and predict atmosphere-watershed interactions over the Great Lakes region. J Adv Model Earth Syst, 12: e2020MS002319

Wang B, Wu R, Lau K (2001). Interannual variability of the Asian summer monsoon: contrasts between the Indian and the western North Pacific–East Asian monsoons. J Clim, 14(20): 4073–4090

Wang C, Liang X Z, Samel A N (2011). AMIP GCM simulations of precipitation variability over the Yangtze River Valley. J Clim, 24(8): 2116–2133

Wang H, Fan K, Sun J, Li S, Lin Z, Zhou G, Chen L, Lang X, Li F, Zhu Y, Chen H, Zheng F (2015). A review of seasonal climate prediction research in China. Adv Atmos Sci, 32(2): 149–168

Wang Q, Robertson D (2011). Multisite probabilistic forecasting of seasonal flows for streams with zero value occurrences. Water Resour Res, 47: W02546

Wang S, Zuo H (2016). Effect of the East Asian Westerly Jet's intensity on summer rainfall in the Yangtze River Valley and its mechanism. J Clim, 29(7): 2395–2406

Wei W, Zhang R, Wen M, Kim B J, Nam J C (2015). Interannual variation of the South Asian High and its relation with Indian and East Asian Summer Monsoon rainfall. J Clim, 28(7): 2623–2634

Wu J, Gao X J (2013). A gridded daily observation dataset over China region and comparison with the other datasets. Chin J Geophys, 56: 1102–1111

Xin X, Wu T, Zhang J, Yao J, Fang Y (2020). Comparison of CMIP6 and CMIP5 simulations of precipitation in China and the East Asian summer monsoon. Int J Climatol, 40(15): 6423–6440

Xu M, Liang X Z, Samel A, Gao W (2014). MODIS consistent vegetation parameter specifications and their impacts on regional climate simulations. J Clim, 27(22): 8578–8596

Xuan S, Zhang Q, Sun S (2011). Anomalous midsummer rainfall in Yangtze River-Huaihe River valleys and its association with the East Asia westerly jet. Adv Atmos Sci, 28(2): 387–397

Yang B, Zhang Y, Qian Y, Huang A, Yan H (2015). Calibration of a convective parameterization scheme in the WRF model and its impact on the simulation of East Asian summer monsoon precipitation. Clim Dyn, 44(5–6): 1661–1684

Yuan X, Liang X Z (2011a). Improving cold season precipitation prediction by the nested CWRF-CFS system. Geophys Res Lett, 38(2): L02706

Yuan X, Liang X Z (2011b). Evaluation of a Conjunctive Surface–Subsurface Process Model (CSSP) over the contiguous United States at regional–local scales. J Hydrometeorol, 12(4): 579–599

Yun Y, Liu C, Luo Y, Liang X, Huang L, Chen F, Rasmmusen R (2020). Convection-permitting regional climate simulation of warm-season precipitation over eastern China. Clim Dyn, 54(3–4):

1469–1489

Zhai P, Zhang X, Wan H, Pan X (2005). Trends in total precipitation and frequency of daily precipitation extremes over China. J Clim, 18(7): 1096–1108

Zhang F, Liang X Z, Li J, Zeng Q (2013). Dominant roles of subgrid-scale cloud structures in model diversity of cloud radiative effects. J Geophys Res Atmos, 118(14): 7733–7749

Zhang S, Lü S, Bao Y, Ma D (2015). Sensitivity of precipitation over China to different cumulus parameterization schemes in RegCM4. J Meteorol Res, 29(1): 119–131

Zhang S, Wang M, Wang L, Liang X Z, Sun C, Li Q (2023). Sensitivity of the simulation of extreme precipitation events in China to different cumulus parameterization schemes and the underlying mechanisms. Atmos Res, 285: 106636

Zhang W, Villarini G, Slater L, Vecchi G A, Bradley A A (2017). Improved ENSO forecasting using bayesian updating and the North American multimodel ensemble (NMME). J Clim, 30(22): 9007–9025

Zhang Y, Chen H (2016). Comparing CAM5 and superparameterized CAM5 simulations of summer precipitation characteristics over continental East Asia: mean state, frequency–intensity relationship, diurnal cycle, and influencing factors. J Clim, 29(3): 1067–1089

Zhao G, Huang G, Wu R, Tao W, Gong H, Qu X, Hu K (2015). A new upper-level circulation index for the East Asian summer monsoon variability. J Clim, 28(24): 9977–9996

Zhu K, Xue M, Zhou B, Zhao K, Sun Z, Fu P, Zheng Y, Zhang X, Meng Q (2018). Evaluation of real-time convection-permitting precipitation forecasts in China during the 2013–2014 summer season. J Geophys Res Atmos, 123(2): 1037–1064